

From the bulge to the outer disc: StarHorse stellar parameters, distances, and extinctions for stars in APOGEE DR16 and other spectroscopic surveys[★]

A. B. A. Queiroz^{1,2}, F. Anders^{3,2,1}, C. Chiappini^{1,2}, A. Khalatyan¹, B. X. Santiago^{4,2}, M. Steinmetz¹, M. Valentini¹, A. Miglio⁵, D. Bossini⁶, B. Barbuy⁷, I. Minchev¹, D. Minniti^{8,9,10}, D. A. García Hernández^{11,12}, M. Schultheis¹³, R. L. Beaton¹⁴, T. C. Beers¹⁵, D. Bizyaev^{16,17}, J. R. Brownstein¹⁸, K. Cunha^{19,20}, J. G. Fernández-Trincado²¹, P. M. Frinchaboy²², R. R. Lane^{23,24}, S. R. Majewski²⁵, D. Nataf²⁶, C. Nitschelm²⁷, K. Pan¹⁶, A. Roman-Lopes²⁸, J. S. Sobeck²⁹, G. Stringfellow³⁰, and O. Zamora¹¹

(Affiliations can be found after the references)

Received 19 December 2019 / Accepted 18 April 2020

ABSTRACT

We combine high-resolution spectroscopic data from APOGEE-2 survey Data Release 16 (DR16) with broad-band photometric data from several sources as well as parallaxes from *Gaia* Data Release 2 (DR2). Using the Bayesian isochrone-fitting code StarHorse, we derived the distances, extinctions, and astrophysical parameters for around 388 815 APOGEE stars. We achieve typical distance uncertainties of ~6% for APOGEE giants, ~2% for APOGEE dwarfs, and extinction uncertainties of ~0.07 mag, when all photometric information is available, and ~0.17 mag if optical photometry is missing. StarHorse uncertainties vary with the input spectroscopic catalogue, available photometry, and parallax uncertainties. To illustrate the impact of our results, we show that thanks to *Gaia* DR2 and the now larger sky coverage of APOGEE-2 (including APOGEE-South), we obtain an extended map of the Galactic plane. We thereby provide an unprecedented coverage of the disc close to the Galactic mid-plane ($|Z_{\text{Gal}}| < 1$ kpc) from the Galactic centre out to $R_{\text{Gal}} \sim 20$ kpc. The improvements in statistics as well as distance and extinction uncertainties unveil the presence of the bar in stellar density and the striking chemical duality in the innermost regions of the disc, which now clearly extend to the inner bulge. We complement this paper with distances and extinctions for stars in other public released spectroscopic surveys: 324 999 in GALAH DR2, 4 928 715 in LAMOST DR5, 408 894 in RAVE DR6, and 6095 in GES DR3.

Key words. stars: distances – stars: fundamental parameters – stars: statistics – Galaxy: general – Galaxy: disk – Galaxy: stellar content

1. Introduction

The second data release (DR2) of the astrometric flagship mission *Gaia* launched by ESA has added an invaluable wealth of astrometric and photometric data for more than a billion stars (Gaia Collaboration 2018). While the DR2 parallax uncertainties are still sufficiently large to hamper detailed tomographic views of the Galaxy beyond 2–3 kpc around the Sun from *Gaia* data alone, the combination of these data with spectroscopic and photometric measurements from various other surveys opens up the possibility of extending the 3D mapping of Galactic stellar populations as far as the Galactic centre and out to similar heliocentric distances towards the outer disc or directions perpendicular to the disc mid-plane. This enables detailed quantitative comparisons between observed properties in phase and chemical space to chemo-dynamical model predictions (e.g. Fragkoudi et al. 2018; Frankel et al. 2018). Additionally, for the first time, ages of large numbers of field stars are being determined with sufficient precision, at least within ≈ 2 kpc, to impose strong direct constraints on the Galactic star formation history (Bensby et al. 2017; Ness et al. 2019).

In Queiroz et al. (2018, Q18), we presented the StarHorse code: a python tool that uses Bayesian analysis of spectroscopic, photometric, and astrometric data to infer distances, extinction, ages, and masses of field stars. In that paper we

illustrated the impact of *Gaia* DR1 parallaxes on improving our estimates of distances and extinctions. We also generated several value-added catalogues (VACs) for the spectroscopic datasets Apache Point Observatory Galaxy Evolution Experiment (APOGEE) DR14 (Abolfathi et al. 2018), Radial Velocity Experiment (RAVE) DR5 (Kunder et al. 2017), the *Gaia*-ESO spectroscopic survey (GES) DR3 (Gilmore et al. 2012), and The GALactic Archaeology with HERMES (GALAH) DR1 (Martell et al. 2017), thus extending the volume for which precise distances are available.

StarHorse has been applied in numerous studies concerning different fields of Galactic astrophysics, such as stellar populations in the local neighbourhood (e.g. Anders et al. 2018; Grieves et al. 2018; Minchev et al. 2018), the origin of the stellar halo (Fernández-Alvar et al. 2017, 2018), the physical carriers of diffuse interstellar bands (Elyajouri & Lallement 2019), Milky Way stellar population kinematics (e.g. Palicio et al. 2018; Monari et al. 2018; Carrillo et al. 2019; Minchev et al. 2019), or recently the chemo-dynamical study of N-rich stars (Fernández-Trincado et al. 2019).

In Anders et al. (2019, A19), we used an updated version of StarHorse, combining *Gaia* DR2 parallaxes and optical photometry with other photometric bands from PanSTARRS-1, 2MASS, and AllWISE, to derive Bayesian distances and extinctions for around 300 million stars brighter than $G = 18$. We showed that the addition of complementary information to the *Gaia* parallaxes and photometry could lead to a breakthrough in which, with the best-quality data, we might start seeing

[★] Data are only available at the CDS via anonymous ftp to cdsarc.u-strasbg.fr (130.79.128.5) or via <http://cdsarc.u-strasbg.fr/viz-bin/cat/J/A+A/638/A76>

structures such as the Galactic bar already in density stellar maps. However, as explained in that paper, the A19 photo-astrometric results were computed with a prior upper limit of 4 mag in A_V extinction, resulting in a limited view of stellar populations towards the innermost regions.

We now have the opportunity to start dissecting the Milky Way, including the central region and the far side of the Galactic disc, by combining *Gaia* DR2 with the APOGEE DR16 release. The latter includes around 380 000 stars with precise radial velocities, stellar parameters, and chemistry from near-infrared (NIR) high-resolution spectra taken in both hemispheres (SDSS-IV Collaboration 2019). Compared to the earlier releases, the data now include many more targets in general, but especially towards the innermost kiloparsecs of the Galaxy.

In this paper we describe the first VACs generated from StarHorse using *Gaia* DR2 data in conjunction with APOGEE DR16 along with public releases of other spectroscopic surveys. We show the first high spatial-resolution chemical maps of our Galaxy covering the entire disc, from 0 to beyond 20 kpc in Galactocentric distance, complementing earlier maps shown in Anders et al. (2014), Hayden et al. (2015), and Weinberg et al. (2019), who used APOGEE DR10, DR12, and DR14, respectively. We presented distances and extinctions, and their associated uncertainties, study the robustness of these quantities to different choices of priors, parameter sets, and systematic corrections, and also compare these quantities to data from other sources.

The paper is organised as follows: in Sect. 2 we provide a brief description of the StarHorse code, focussing on the main improvements since Q18 and A19. Section 3 describes the input data (photometry, astrometry, and spectroscopy) used in the computations of distances and extinctions for APOGEE DR16. In Sect. 4 we describe the output parameters that resulted from the StarHorse calculation as well as their uncertainties. As an example of science application, in Sect. 5 we present the first density and chemical maps obtained over the entire Galactic plane and discuss the main science implications derived from these maps. In Sect. 6 we discuss the complementary catalogues GALAH, RAVE, GES, and the Large Sky Area Multi-Object Fiber Spectroscopic Telescope (LAMOST), and the distribution of the resulting parameters. The resulting catalogues are provided in machine-readable form: the data model can be found in Appendix A, a set of validation tests that for our new StarHorse APOGEE DR16 results can be found in Appendix B, and summary plots for each survey are shown in Appendix C. In Sect. 7 our main conclusions are summarised.

2. StarHorse code

StarHorse (sometimes abbreviated as SH in the resulting catalogues) is a Bayesian isochrone-fitting code that derives distances d , extinctions in the V band (at $\lambda = 542$ nm) A_V , ages τ , masses m_* , effective temperatures T_{eff} , metallicities $[M/H]$, and surface gravities $\log g$ for field stars. In order to do so, we use as input a set of spectroscopically measured stellar parameters (typically T_{eff} , $\log g$, and metallicity $[M/H]$), photometric magnitudes m_λ , and, when available, parallax ϖ , to estimate how close a stellar evolutionary track is to the observed data. In this work we adopt the latest version of the PARSEC stellar evolutionary model tracks (Bressan et al. 2012; Marigo et al. 2017)¹. For APOGEE DR16 we adopt a fine grid of models to compute the estimated parameters with steps of 0.01 dex in $\log \tau$ and 0.02 dex

in metallicity $[M/H]$, covering the ranges $7.5 < \log \tau < 10.13$, $-2.2 < [M/H] < 0.6$.

To compute the posterior probability distribution function (PDF) for the model parameters given the observed data, we include priors about the geometry, metallicity, and age characteristics of the main Galactic components, following previous Bayesian methods to derive distances (e.g. Burnett & Binney 2010; Burnett et al. 2011; Binney et al. 2014). The priors adopted are the same as in Q18 and A19, namely: an initial mass function from Chabrier (2003) for all Galactic components; exponential spatial density profiles for thin and thick discs (see Sect. 5 for a discussion on the differences between the geometric and chemical definitions of the thick disc); a spherical halo and a triaxial (ellipsoid + spherical) bulge/bar component, and broad Gaussians for the age and MDF priors. The normalisation of each Galactic component, as well as the solar position, were taken from Bland-Hawthorn & Gerhard (2016).

The code was first described in Santiago et al. (2016), and later modified to use *Gaia* parallaxes and derive astrophysical stellar parameters in Queiroz et al. (2018). The latter paper also included extensive validation comparisons with simulations and independent high-quality distance determinations from astero-seismology, eclipsing binaries, and open clusters. Those samples showed precision of $\approx 10\%$ for distances, ages accurate to $\approx 30\%$, and A_V errors of ≈ 0.1 mag for stars out to ≈ 1 kpc, with a continuous worsening of accuracy and precision towards larger distances. Most recently, in A19, we used StarHorse to determine photo-astrometric (i.e. not using spectroscopy at all) distances, extinctions, and stellar parameters for *Gaia* DR2 stars down to magnitude $G = 18$.

More details about the method, priors, stellar evolutionary models, code validation, and previous released catalogues are provided in Q18. We have since updated the code in some important aspects briefly summarised in this work (for more details see A19). Namely, we improved the extinction treatment, which now considers the dependence of the extinction coefficient, A_λ , on effective temperature and extinction itself, as explained in Holtzman et al. (1995), and Girardi et al. (2008), for instance; and the latest version has migrated to python 3.6, which made the code faster and compatible with recent libraries. These and other small computational improvements are described in detail in A19, Sect. 3.2. In this paper, we use the high-quality spectroscopically determined stellar parameters from APOGEE spectra, in conjunction with *Gaia* DR2 parallaxes and broad-band photometric measurements.

3. Input data

We followed a similar configuration to previous StarHorse runs (Queiroz et al. 2018; Anders et al. 2019) to complement the APOGEE DR16 StarHorse catalogue with parameters such as extinction and distances. We gathered parallaxes from *Gaia* DR2 (Gaia Collaboration 2018) and photometry from 2MASS (Cutri et al. 2003), WISE (Cutri et al. 2013), and PanSTARRS-1 (Chambers et al. 2016) and gathered this information with spectra from APOGEE DR16 (SDSS-IV Collaboration 2019). We introduced the input catalogues, the necessary adjustments in these data, and the StarHorse configuration to produce the final parameters.

3.1. APOGEE DR16

The spectroscopic survey APOGEE (Majewski et al. 2017) started in the third phase of the Sloan Digital Sky Survey

¹ Downloaded from <http://stev.oapd.inaf.it/cgi-bin/cmd>

(SDSS-III; Eisenstein et al. 2011). The APOGEE survey continues as part of SDSS-IV (Blanton et al. 2017). It is a spectroscopic survey conducted in the NIR, at high resolution ($R \sim 22\,500$), and high signal-to-noise ($S/N > 100$) (Wilson et al. 2019). The data reduction pipeline is described in Nidever et al. (2015). As a NIR survey, APOGEE is capable to peer into the dusty areas of our Galaxy, such as the Galactic bulge and the central Galactic plane.

The APOGEE survey has been collecting data in the northern hemisphere since 2011. Since 2015, APOGEE-2 data have also been collected in the southern hemisphere. Observations from both hemispheres use the twin NIR spectrographs (Wilson et al. 2019) on the SDSS 2.5 m telescope at APO (Gunn et al. 2006) and the 2.5 m du Pont telescope at Las Campanas Observatory (LCO; Bowen & Vaughan 1973), respectively. The DR16 is the first SDSS-IV data release that includes data from APOGEE-2 South: it contains a total of 473 307 sources with derived atmospheric parameters and abundances. The pre-processing of the APOGEE DR16 data in preparation for the StarHorse run presented in this work was very similar to the pre-processing of APOGEE DR14 described in Q18.

The APOGEE Stellar Parameter and Chemical Abundance Pipeline (ASPCAP; García Pérez et al. 2016) was optimised for red giant stars, since this is the main population targeted by the survey. However, we also computed StarHorse results for stars in APOGEE DR16 catalogue that fall outside the recommended calibration ranges of ASPCAP. For those stars we used inflated uncertainties of $\sigma_{\log g} = 0.3$ dex, $\sigma_{T_{\text{eff}}} = 200$ K, $\sigma_{[\text{Fe}/\text{H}]} = 0.15$ dex, and $\sigma_{[\alpha/\text{Fe}]} = 0.1$ dex.

As in Q18 (and differently from A19 where no extinction prior was used), we used the APOGEE targeting extinction estimate $A_{K_s}^{\text{Targ}}$ as a broad prior for the total line-of-sight extinction: $A_{V_{\text{prior}}} = 0.11 \cdot A_{K_s}^{\text{Targ}}$. StarHorse treats this extinction using Schlafly et al. (2016) extinction curve.

Finally, because we used PARSEC stellar models, which at present do not include non-solar $[\alpha/\text{Fe}]$ ratio models, we corrected for this effect in the input data. For that we used the Salaris et al. (1993) formula, which accounts for α -enhancement by a slight shift of the total metallicity $[\text{M}/\text{H}]$ as follows:

$$[\text{M}/\text{H}] = [\text{Fe}/\text{H}] + \log [C \cdot 10^{[\alpha/\text{Fe}]} + (1 - C)] \quad (1)$$

$$\sigma_{[\text{M}/\text{H}]} \approx \sqrt{\sigma_{[\text{Fe}/\text{H}]}^2 + \sigma_{[\alpha/\text{Fe}]}^2}. \quad (2)$$

We chose $C = 0.66101$, in agreement with the scaled solar composition $Y = 0.2485 + 1.78 \cdot Z$ used in the PARSEC 1.2S models².

3.2. Gaia Data Release 2

The *Gaia* astrometric mission was launched in December 2013 and placed close to the L2 Lagrangian point, about 1.5 million km from the Earth, in July 2014. It is measuring positions, parallaxes, proper motions, and photometry for well over 10^9 sources down to $G \approx 20.7$, and obtaining physical parameters and radial velocities for millions of brighter stars (Gaia Collaboration 2016). Its recent Data Release 2 (*Gaia* DR2; Gaia Collaboration 2018) covers the initial 22 months of data taking (from a predicted total of >5 years) and has positions and photometry for 1.7×10^9 sources, full astrometric solutions for 1.3×10^9 (Lindgren et al. 2018), T_{eff} , extinction, stellar radii and luminosities for 8×10^7 stars (Andrae et al. 2018), and radial

velocities for 7×10^6 of the sources (Katz et al. 2019). Particularly important for our purposes are the DR2 parallaxes, since they allow us to better disentangle dwarfs from giants for stars with more uncertain surface gravity measurements.

The *Gaia* DR2 parallax precision varies from <0.03 mas for $G \leq 13$ to ≈ 0.7 mas for $G = 20$, and the parallax zero-point (accuracy) has been shown to be of similar order, and probably dependent on a combination of sky position, magnitude, and colour (e.g. Arenou et al. 2018; Stassun & Torres 2018; Zinn et al. 2019; Khan et al. 2019).

In this work, we adopted the mean zero-point correction of $52.8 \mu\text{as}$ to the *Gaia* DR2 parallaxes determined by Zinn et al. (2019) using red giants co-observed by APOGEE and the *Kepler* mission. This is somewhat midway between the quasar-derived correction advertised by Lindgren et al. (2018) and the zero-point shift estimated by Stassun & Torres (2018), which is $82 \mu\text{as}$. In fact, Stassun & Torres (2018) find that their estimate of the offset may be $61 \mu\text{as}$, which is much closer to that of Zinn et al. (2019), if they allow for a possible scale error in the parallaxes. They also note that the larger offset of $82 \mu\text{as}$ would be most applicable to the brightest stars, with $G \lesssim 11$, however only $\sim 10\%$ of the APOGEE sample is so bright. On the other hand, Khan et al. (2019) find that the parallax zero-point shift could be smaller: for two *K2* fields analysed in their paper they find smaller discrepancies between asteroseismic and astrometric parallaxes than in the *Kepler* field.

Independent distances measurements using cepheids and quasars (Riess et al. 2018; Lindgren et al. 2018) also show that the *Gaia* DR2 parallax uncertainties are slightly underestimated, and can suffer from systematics as well as the parallax itself. To account for these effects we applied the suggested inflation of parallax uncertainties described in Lindgren et al. (2018). The inflated error can be written as

$$\sigma_{\text{ext}} = \sqrt{k\sigma_{\text{in}}^2 + \sigma_s^2}, \quad (3)$$

where σ_{ext} is the inflated uncertainty, σ_{in} the uncertainty from *Gaia* catalogue, $k = 1.08$ is a constant parameter, and σ_s is slightly different for different magnitude ranges. For the bright regime ($G < 13.0$ mag) we used $\sigma_s = 0.021$ and for the faint regime ($G > 15.0$ mag) we used $\sigma_s = 0.043$. In between these two regimes we interpolated linearly using $\sigma_s = 0.030$.

The *Gaia* DR2 catalogue also includes broad-band photometry for about 10^9 sources, although in the case of APOGEE we decided not to include this photometry in the calculations. The reason for this choice is simply because most of APOGEE DR16 is targeting the Galactic plane, and in this region *Gaia* DR2 photometry partly suffers from crowding issues. In addition, it should be acknowledged that the *Gaia* DR2 photometry for the G_{BP} and G_{RP} bands is essentially aperture photometry, which has been shown to be problematic in regions of high stellar density and/or nebulous emission (e.g. Evans et al. 2018; Arenou et al. 2018). We therefore followed a conservative approach and did not use this photometry for the APOGEE sample.

3.3. Photometric catalogues

In all produced catalogues we use infrared photometry from 2MASS (Cutri et al. 2003) and WISE (Cutri et al. 2013). Both are all-sky photometric surveys, and 2MASS photometry has almost 100% coverage of the APOGEE catalogue. For that reason we used it as primary photometry when running StarHorse (see Q18 details). For both input catalogues, we applied a minimum photometric uncertainty of 0.03 mag. Finally, we assumed

² http://stev.oapd.inaf.it/cgi-bin/cmd_3.1



Fig. 1. One-dimensional distributions and correlations between StarHorse output parameters (*bottom left corner plot*) and their corresponding uncertainties (*top right corner plot*) for the APOGEE DR16 sample.

the uncertainty of the stars in 2MASS and WISE, which have no measured uncertainty to be 0.4 mag.

For the optical regime we used PanSTARRS-1 photometry ($\lambda \sim 3943\text{--}10\,838 \text{ \AA}$) (Scolnic et al. 2015) with corrected zero points according to Scolnic et al. (2015) and minimum photometric uncertainties of 0.04 mag. Furthermore, we only used measurements with reported individual errors for stars fainter than $G = 14.5$.

In contrast to Q18, we decided only to use PanSTARRS-1 photometry rather than APASS (Henden & Munari 2014) photometry. The motivation for this choice comes from reports that APASS photometry has a high percentage of sources (30%) with a positional mismatch, especially in the faint regime ($g_{\text{sloan}} > 16$) (Marrese et al. 2019).

4. APOGEE DR16 StarHorse catalogue

The APOGEE DR16 StarHorse catalogue presented in this work was generated from the processed APOGEE DR16 data, explained in Sect. 3.1, cross-matched with *Gaia* DR2 (98%), PanSTARRS-1 (37%), 2MASS (100%), and AllWISE (95%). The final produced catalogue contains 388 815 unique stars with derived StarHorse parameters, along with their uncertainties. From the 473 307 APOGEE sources StarHorse has converged for 418 715, and after this we selected unique stars by the highest signal to noise.

Our catalogue will appear as a VAC of the SDSS DR16 (SDSS-IV Collaboration 2019). The catalogue can also be downloaded from Leibniz Institute for Astrophysics (AIP) webpage³,

³ <https://data.aip.de/aqueiroz2020>

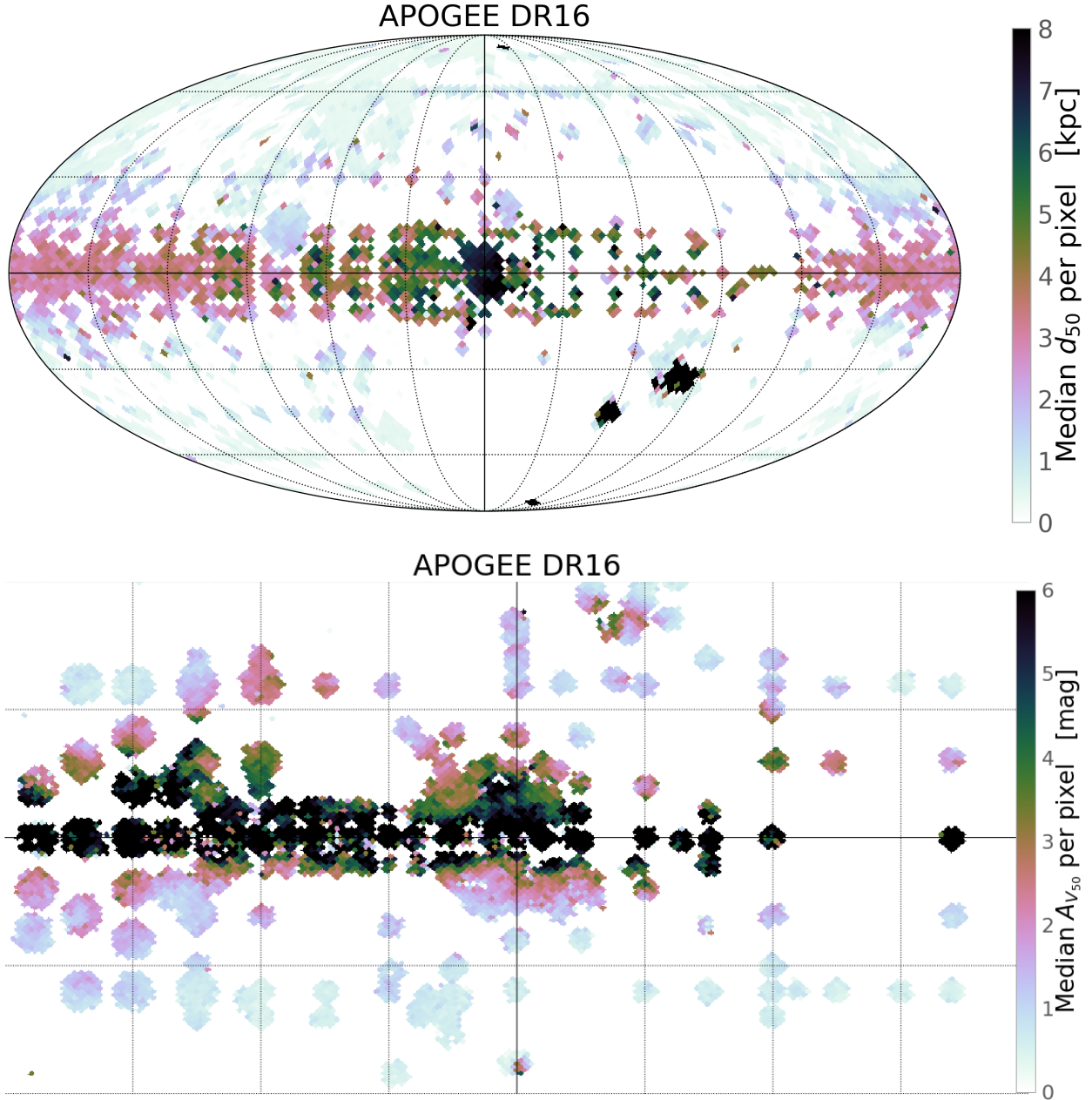


Fig. 2. Overview of the coverage of the APOGEE DR16 StarHorse VAC. *Top panel:* median StarHorse distance per HealPix cell as a function of Galactic coordinates. *Bottom panel:* same as in previous panel, but now showing the median A_V as a function of direction in the sky, and zooming in on the innermost $40 \times 20^\circ$ of the Galactic plane (the line spacing in the *bottom panel* is 10°).

similar to what was done in Q18. The description and format of the provided StarHorse products are listed in Table A.1, while the description of the adopted input and output quality flags can be found in Table A.2.

The StarHorse output provides the posterior distribution functions of masses, effective temperatures, surface gravity, metallicities, distances, and extinctions (see Table A.1). The median value 50th percentile should be taken as the best estimate for that given quantity and the uncertainty can be determined using the 84th and 16th percentiles. The full distribution of the StarHorse median output parameters is shown in the left panel of Fig. 1.

In addition to the percentile values of the estimated parameters, all released VACs have columns that describe the StarHorse input data, SH_INPUTFLAGS, and the StarHorse

output data, SH_OUTPUTFLAGS as specified in Table A.1. The input flags describe which parameters were used in the likelihood calculation for each star. These flags also indicate if we used an A_V prior as the A_V prior flag or if the A_V was determined using the parallax True option (see Q18). The meaning of each string in SH_INPUTFLAGS can be seen in Table A.2. The output flags inform the number of models which have converged in the likelihood calculation and also indicate the occurrence of problems in the estimated extinction (see also Table A.2).

In what follows we present some of the basic properties of the APOGEE-DR16 StarHorse catalogue (maps involving chemical abundances are discussed in the next section). In the following figures we applied a few quality cuts as follows: stars with signal-to-noise ratio greater than 50 ($\text{SNREV} > 50$), those with non-negative posterior extinction ($A_{V_{84}} > 0$), and those with

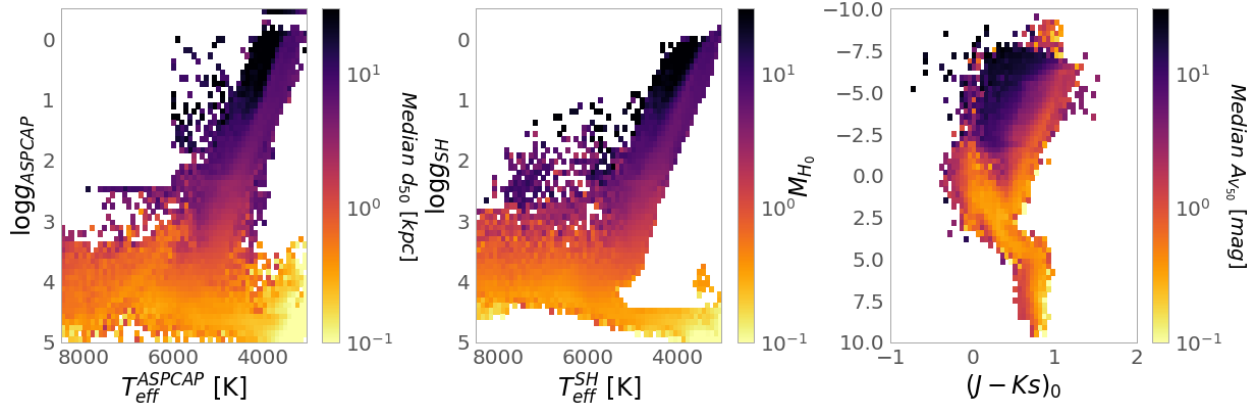


Fig. 3. Kiel diagram colour coded by median StarHorse distance as a function of position on the input (*left*) and output (*middle*) effective temperatures and surface gravities. *Right-most panel:* colour magnitude diagram coloured by median StarHorse extinction; the colour is already corrected by StarHorse extinction.

APOGEE DR16: Impact of input parameters

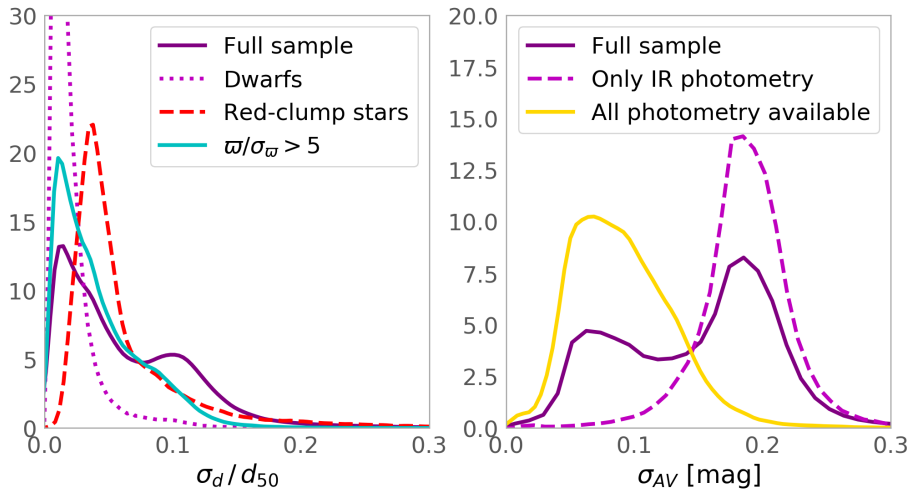


Fig. 4. Kernel-density estimates of the uncertainty distributions for the distances (*left panel*) and A_V extinctions (*right panel*) in the APOGEE DR16 StarHorse VAC. The different curves show the distributions of distances and extinctions uncertainties for subsets of different data input quality. *Left panel:* we highlight the higher distance precision achieved for *a* stars with *Gaia* DR2 parallaxes more precise than 20%, *b* dwarf stars ($\log g < 4$), and *c* red-clump stars ($2.3 < \log g < 2.5$). In the *right panel*, we show how the (un-)availability of optical photometry drastically improves or worsens the precision of our A_V estimates.

a good ASPCAP fit (ASPCAP_CHI2 < 25). This corresponds to $\approx 95\%$ of the converged stars.

Figure 2 shows Galactic maps colour coded by the median of the resulting APOGEE DR16 StarHorse distances (top panel) and extinctions (middle panel). By design, most of the APOGEE pointings are concentrated towards low Galactic latitudes (Zasowski et al. 2013, 2017), offering a much greater coverage of the thin disc than other surveys. The north-south equatorial asymmetry is also visible, since most of the data so far come from the northern spectrograph at Apache Point Observatory. Yet, the Magellanic Clouds are clearly visible on the distance map as the distant clumps of sampled stars. Because the density of stars increases towards the Galactic centre, there is also a clear trend of larger median distances in this direction. The A_V map in the bottom panel of Fig. 2 zooms into the central degrees of the Galactic plane, where the average extinction is higher, and patchy (also visible in this map).

Figure 3 shows the mean distance per pixel in the spectroscopic Kiel diagram, using the input parameters from APOGEE (ASPCAP; left panel) and using the StarHorse output spectroscopic parameters (middle panel). As expected, stars belonging to the giant branch (comprising most of the APOGEE sample) are found at larger distances than dwarfs since they have brighter absolute magnitude and are therefore detectable in a larger distance range. In the giants regime StarHorse seems

to be detecting asymptotic giant branch stars (AGBs) at very large distances (at $T_{\text{eff}} \sim 4500$ K and $\log g < 1.0$), as expected since those are very bright stars. However, those stars should be analysed with care since the ASPCAP pipeline does not perform well in this range (García Pérez et al. 2016). The third panel of Fig. 3 also shows higher extinction for intrinsic brighter and therefore distant stars. The output spectroscopic parameters from StarHorse seem to be, as expected, very much in accordance with the input ASPCAP parameters. For the dwarfs stars, which are not ASPCAP calibrated stars and therefore have larger uncertainties, StarHorse seems to improve the results finding a smoother solution, as expected because of the use of stellar evolutionary models.

The distribution of distance and extinction uncertainties for the APOGEE DR16 StarHorse catalogue are shown in Fig. 4. Thanks to the availability of *Gaia* DR2 parallaxes, the distance uncertainties (left panel of Fig. 4) are usually smaller than 10%. The three peaks at $\approx 2\%$, 4% , and $\approx 10\%$ correspond to nearby dwarf stars within the *Gaia* DR2 parallax sphere, red-clump stars, and more distant giant stars, respectively. These distance uncertainties are slightly improved with respect to those from the DR14 APOGEE and *Tycho-Gaia* astrometric solution (TGAS) sample discussed in Q18, but now are available for a much larger number of stars, covering much larger volumes. Even for distant upper red-giant branch stars with more uncertain parallaxes (e.g.

APOGEE targets near the Galactic centre), the achieved distance precision is typically within 10%.

The extinction uncertainty distribution (right panel of Fig. 4) is clearly double-peaked, at $A_V \simeq 0.07$ and $A_V \simeq 0.17$, as previously observed by Q18 for APOGEE DR14 combined with TGAS. As shown by the two subsets in the figure, the two peaks correspond to stars with and without available optical magnitudes, respectively. A more detailed discussion of the accuracy of the obtained parameters can be found in Appendix B.

In Fig. 1 we show the correlations between the output parameters and the correlations between the output uncertainties. We see the expected correlations between stellar parameters inherited from the isochrones (e.g. the $\log g$ versus T_{eff} diagram), as well as stellar population effects, such as the decrease of $\log g$ with increasing distance or a greater metallicity range for greater distances. Extinction is correlated with increasing mass, metallicity, and distance. The doubled-peaked uncertainty distribution in extinction is not explained by any other output parameter uncertainty apart from the completeness of the photometric set as seen in Fig. 4. The uncertainties in the other parameters show approximately linear correlations between $\log g$ and mass, $\log g$ and distance, as well as mass and distance. The distribution of each parameter and its uncertainty can also be seen in the diagonal row of that plot, along with the uncertainty statistics for each of the StarHorse output parameters.

5. Extended chemical maps in the Galactic plane up to the bulge

In this section, we demonstrate the value of the APOGEE DR16 StarHorse results by presenting the most extensive and precise chemical-abundance map of the Milky Way disc and bulge to date. The unprecedented coverage of the APOGEE DR16 data can be appreciated in Fig. 5, in which we show the density distribution of all DR16 stars with StarHorse results in galactocentric coordinates in galactocentric coordinates. In this figure the colour represents the 3D local stellar density estimated via the smoothed-particle technique (Monaghan 1992) with $N_{\text{ngb}} = 35$ neighbours; the maximum intensity projection rendering method implemented in `pmviewer`⁴ is used.

Figure 5 shows very clearly that the APOGEE DR16 sample covers a large portion of the Galaxy with statistically significant samples; these now include the innermost regions with many more stars close to the Galactic mid-plane ($Z_{\text{Gal}} < 0.5$ kpc) thanks to the southern observations taken at Las Campanas. This is an important improvement in the number of targets and in the quality of distances and extinction estimates with respect to previous releases.

To be more quantitative, the stellar density of the APOGEE DR16 sample amounts to over a thousand stars per kpc^2 in the complete $R_{\text{Gal}}-Z_{\text{Gal}}$ plane for $0 < R_{\text{Gal}} < 15$ kpc and $-1 \text{ kpc} < Z_{\text{Gal}} < 1$ kpc (see Fig. 5), allowing for an unprecedented chemo-kinematic mapping of the inner and outer stellar disc. The top panel of Fig. 5 displays a top-down view of the Galactic disc, again demonstrating the exquisite spatial coverage of the APOGEE DR16 sample. The figure also shows a slight but distinct density enhancement in the region of the stellar bar, as observed for the full *Gaia* DR2 dataset in Anders et al. (2019), but with the canonical inclination angle of $\sim 25^\circ$ (e.g. Bland-Hawthorn & Gerhard 2016).

Since APOGEE traces around 20 chemical elements at high spectral resolution and provides radial velocities precise to

$\sim 300 \text{ m s}^{-1}$ (Majewski et al. 2017), this dataset will be a legacy for detailed chemo-dynamical studies of the Milky Way at least for several years.

To illustrate the impact of the APOGEE data released with the 16th SDSS Data Release in the field of Galactic archaeology, we focus on just a few examples of abundance-ratio maps in bins of galactocentric cylindrical coordinates ($R_{\text{Gal}}, Z_{\text{Gal}}$), in a similar manner as the maps presented by Hayden et al. (2015) using DR12 data: first, the standard relative-to-iron abundance diagrams (Figs. 6 and 7 for $[\alpha/\text{Fe}]$ versus $[\text{Fe}/\text{H}]$ and Fig. 8 for $[\text{Al}/\text{Fe}]$ versus $[\text{Fe}/\text{H}]$); and second, two examples of an abundance ratio as a function of an alpha-element ($[\text{Mg}/\text{O}]$ versus $[\text{Mg}/\text{H}]$ and $[\text{Al}/\text{Mg}]$ versus $[\text{Mg}/\text{H}]$, shown in Fig. 9). These figures show, for different bins of R_{Gal} and Z_{Gal} , diagrams of abundances colour coded by density estimation using a Gaussian kernel. The bandwidths of the kernel density estimates obey Scott's rule (Scott 1992). Figures 6 and 7 also show, in the top plots, the uncertainty distributions in distance and extinction for each R_{Gal} bin.

Owing to the pencil-beam nature of the APOGEE survey, and the fact that metal-poor stars are brighter, the relative weight of the sub-populations in each plot may still be slightly affected by the selection function. Therefore, a quantitative interpretation of these spatial chemical maps needs to take into account such biases and will be the subject of future work. The so-called α elements are produced by core-collapse supernovae and hence more directly connected with the star formation rate. Recently, Weinberg et al. (2019) discussed such abundance maps, but based on a much smaller sample of $\sim 20\,000$ stars from APOGEE DR14, and not including data in the innermost radial bin ($0-2$ kpc), which is now possible.

5.1. Map of $[\alpha/\text{Fe}]$ versus $[\text{Fe}/\text{H}]$

The $[\alpha/\text{Fe}]$ versus $[\text{Fe}/\text{H}]$ diagram has long served as a tracer of the chemical enrichment timescales of the Milky Way (Matteucci 2012), which are a consequence of the star formation history. A pioneer work to demonstrate the direct connection of the high- $[\alpha/\text{Fe}]$ ‘‘plateau’’ with old stars was realised by Fuhrmann (1998, 2011), who computed ages for a volume-complete sample of HIPPARCOS stars within 25 pc of the Sun. His work clearly showed the stars on the high- $[\alpha/\text{Fe}]$ plateau to be older than 10 Gyr, whereas stars along the chemical thin-disc sequence were found to be younger. The observed chemical discontinuity in the $[\alpha/\text{Fe}]$ versus $[\text{Fe}/\text{H}]$ diagrams in the solar neighbourhood has important consequences on interpretations related to the assembly history of the Milky Way and similar galaxies (see e.g. Chiappini et al. 1997; Minchev et al. 2013; Mackereth et al. 2018; Buck 2020; Nuza et al. 2019; Spitoni et al. 2019 for discussions).

The mapping of the Milky Way in terms of the $[\alpha/\text{Fe}]$ vs. $[\text{Fe}/\text{H}]$ diagram has quickly evolved since then. The first high-resolution spectroscopic samples outside the solar vicinity were small and without age information (e.g. Bensby et al. 2010, 2011; Alves-Brito et al. 2010 – see Fig. 14 of Anders et al. 2014), but were already able to show the complexity and impact of such maps. For instance, the disappearance of high- $[\alpha/\text{Fe}]$ stars towards the outer disc could be interpreted as an indication that the (chemical) thick disc had a shorter scale length than the thin disc (Bensby et al. 2011; Cheng et al. 2012), contrary to what had been seen for the (geometrically defined) thick discs in other galaxies.

Extended maps, with a much better coverage along the Galactic mid-plane ($|Z_{\text{Gal}}| < 0.5$ kpc) only appeared with

⁴ <http://pmviewer.sourceforge.net>

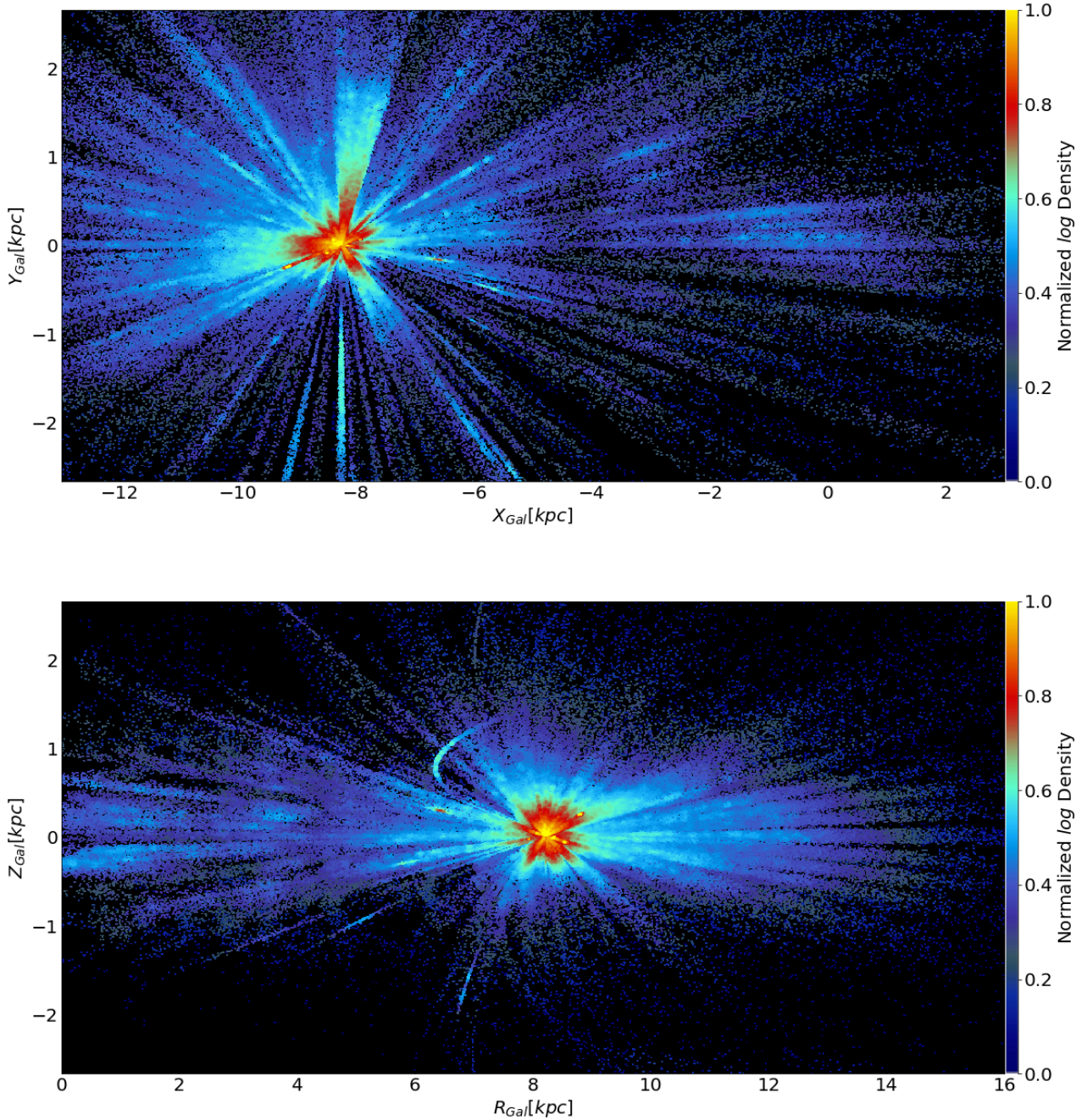


Fig. 5. *Top panel:* galactocentric Cartesian XY map of the APOGEE DR16 sample. *Bottom panel:* density distribution in Galactocentric cylindrical RZ coordinates. Some distinct features of APOGEE targeting can be easily discerned: the high target density in the *Kepler* field, enhanced density distributions around open clusters. These are sometimes elongated when the distance precision is low, e.g. ($d \sim 5.2$ kpc); ω Cen appear around $R \approx 6.5$ kpc, $Z \approx 1$ kpc.

APOGEE (Allende Prieto et al. 2008; Majewski et al. 2017), which in its first year of data (with around only 20 000 stars of sufficient quality) was already able to demonstrate that the chemical discontinuity observed by Fuhrmann was also present far outside the solar neighbourhood (Anders et al. 2014; Nidever et al. 2014), also confirming the short scale length of the chemical thick disc. These APOGEE results were complemented by other surveys at larger distances from the Galactic mid-plane (e.g. Bovy & Rix 2013; Mikolaitis et al. 2014, and references therein), but without such a good coverage of the inner Galaxy.

Shortly afterwards, Hayden et al. (2015) used a sample of around 70 000 red giants from APOGEE DR12 (Alam et al.

2015) to increase the sampled volume with respect to the 2014 maps, covering a Galactocentric distance range between 3 kpc and 15 kpc within 2 kpc of the Galactic plane. By that time it became clear that towards the outer parts of the disc we would see a flaring, in which the low- $[\alpha/\text{Fe}]$ would dominate even at large heights above the Galactic mid-plane (see Minchev et al. 2015, 2019 for discussions), implying that the term “thick disc” should be used more carefully. The chemically defined thick disc (by separating populations in the $[\alpha/\text{Fe}]$ versus $[\text{Fe}/\text{H}]$ diagram) is indeed confined to the inner regions, whereas the geometrically defined thick disc (by a cut in Z_{Gal}) is a mixture of flaring mono-age populations, and therefore would show an

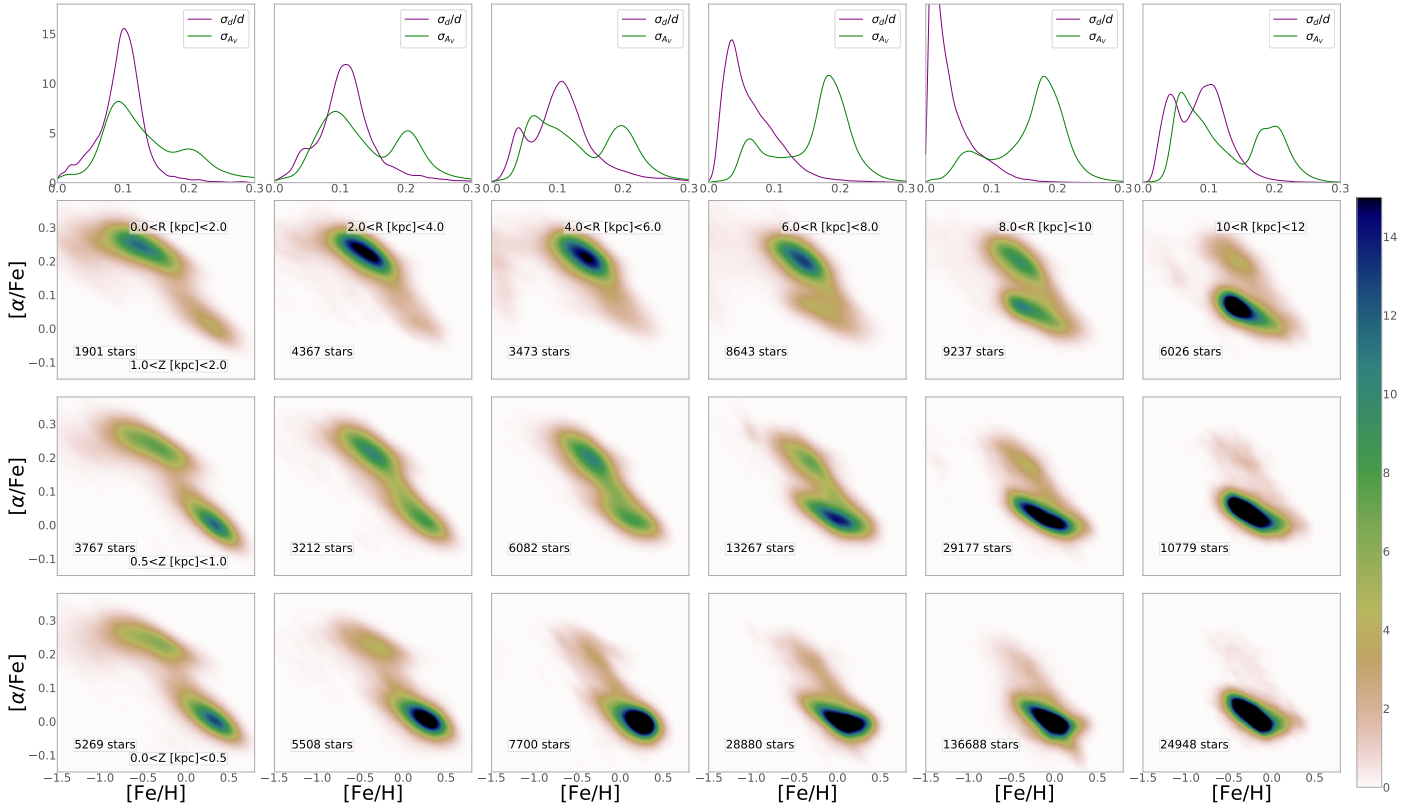


Fig. 6. APOGEE DR16 $[\alpha/\text{Fe}]$ vs. $[\text{Fe}/\text{H}]$ diagrams in bins of galactocentric cylindrical coordinates, similar to the chemical maps presented in Hayden et al. (2015), but extending further into the inner Galaxy. *Top panels:* kernel-density estimates of the uncertainties distributions in StarHorse extinctions and distances, for each galactocentric distance bin (including all Z_{Gal} bins).

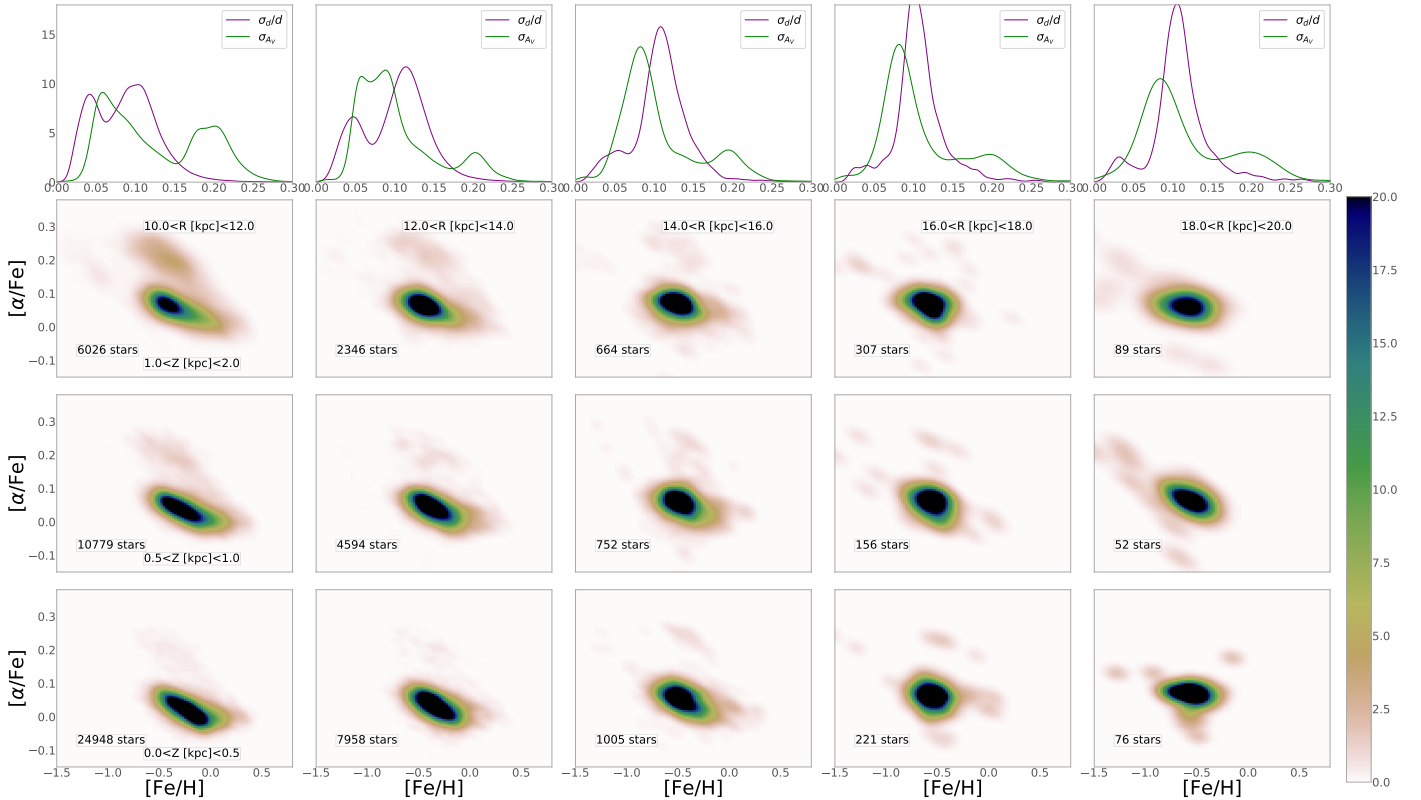


Fig. 7. Same as previous figure, but now extending to the outer disc.

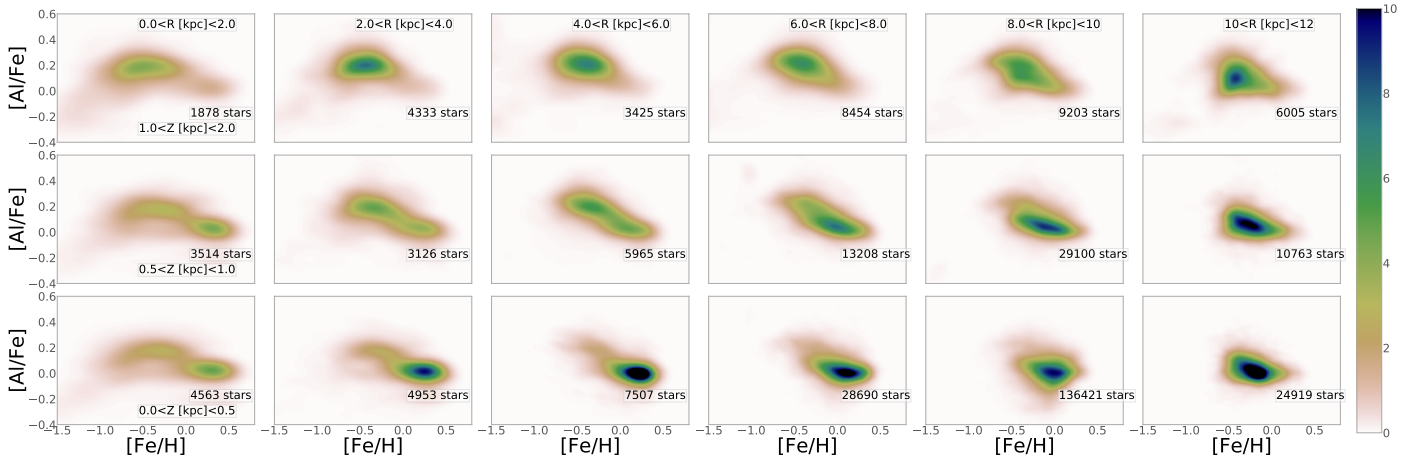


Fig. 8. APOGEE DR16 $[\alpha/\text{Fe}]$ vs. $[\text{Fe}/\text{H}]$ diagrams in bins of galactocentric cylindrical coordinates out to $R_{\text{Gal}} = 10$ kpc, similar to Fig. 6.

age gradient (see [Martig et al. 2016](#); [Mackereth et al. 2017](#); [Minchev et al. 2018](#)).

The [Hayden et al. \(2015\)](#) chemical-abundance maps were limited by the still poor coverage of the innermost parts of the Milky Way. That paper, along with following APOGEE publications (e.g. [Zasowski et al. 2019](#) based on DR14) tentatively reported that stars with $R_{\text{Gal}} < 5$ kpc seem to lie on a single track, whereas at larger radii two distinct sequences were observed (an observation later interpreted as the fundamental dichotomy between the inner and outer discs by [Haywood et al. 2016, 2018](#)). [Recio-Blanco et al. \(2017\)](#), using a sample of GES spectra, report the existence of low- $[\alpha/\text{Fe}]$ in the bulge area. With the larger APOGEE sample available from SDSS DR14 ([Abolfathi et al. 2018](#)), [Rojas-Arriagada et al. \(2019\)](#) selected stars within 3.5 kpc from the Galactic centre and report the detection of a bimodal sequence in $[\text{Mg}/\text{Fe}]$ versus $[\text{Fe}/\text{H}]$, confirming the GES results. The authors also suggest the two sequences to merge above $[\text{Fe}/\text{H}] \sim 0.15$ dex into a single sequence (see [Barbuy et al. 2018](#) for a review of other chemical-abundance studies of the Galactic bulge previous to APOGEE DR14 and *Gaia* DR2).

Figures 6 and 7 present our updated $[\alpha/\text{Fe}]$ versus $[\text{Fe}/\text{H}]$ diagrams in 2 kpc bins in width in R_{Gal} and three narrow bins in $|Z_{\text{Gal}}|$, obtained from APOGEE DR16 in combination with *Gaia* DR2 and our StarHorse distances. These abundance-ratio maps now extend from $R_{\text{Gal}} = 0$ out to 20 kpc, with excellent statistics (more than 150 stars per bin) out to $R_{\text{Gal}} = 18$ kpc, where the target density drops dramatically. To avoid figures that are too crowded, we divided the chemical-abundance maps into two plots: Fig. 6 shows the $[\alpha/\text{Fe}]$ versus $[\text{Fe}/\text{H}]$ diagrams for the inner-disc bins, while Fig. 7 shows the outer-disc bins. The distance and extinction uncertainties in each of the radial bins are shown in the top row of the two figures. These show that even in the innermost 2 kpc, StarHorse achieves precision of around 10% in distance and better than 0.1 mag in A_V for most of the targets; the, unfortunately, less precise extinction estimates in regions closer to the solar position is due to our imposed bright limit for the Pan-STARRS1 photometry.

While the DR16 $[\alpha/\text{Fe}]$ versus $[\text{Fe}/\text{H}]$ diagrams shown in Figs. 6 and 7 confirm most of the previous analyses, they also show some clear and important differences. Figure 6 now shows a much more complete view of the chemical-abundance distribution in the inner disc. Each of the innermost bins ($R_{\text{Gal}} < 4$ kpc) contains more than 1000 stars now, and especially very close to the Galactic mid-plane these numbers amount to >5000 (see the

two leftmost bottom panels), potentially also allowing for analyses of azimuthal abundance variations.

The bimodality reported by [Rojas-Arriagada et al. \(2019\)](#) is clearly confirmed in this improved map: we observe this bimodality in all $[\alpha/\text{Fe}]$ – $[\text{Fe}/\text{H}]$ diagrams in the innermost regions ($R_{\text{Gal}} < 4$ kpc), but especially for stars closest to the Galactic plane ($|Z_{\text{Gal}}| < 0.5$ kpc). The single sequence reported in [Hayden et al. \(2015\)](#) and [Zasowski et al. \(2019\)](#) for the innermost regions is not confirmed now, as the bins at lower $|Z_{\text{Gal}}|$ contain more data.

In contrast to [Rojas-Arriagada et al. \(2019\)](#), however, the two blobs completely define the detached sequences without merging, thus showing a true chemical discontinuity. The new maps show that the chemical discontinuity seen in the solar neighbourhood bin (mostly studied by other surveys; middle row, fourth column) extends towards the bulge and become completely separated; this is very similar to what was found by [Fuhrmann \(1998, 2011\)](#), within 25 pc but now extended to larger metallicities, as expected given the observed abundance gradients in the Galactic disc. The more detailed implications of these maps for chemo-dynamical models of the Milky Way will be discussed in future papers. We also caution that this chemical discontinuity is not seen in smaller samples of bulge stars (e.g. [da Silveira et al. 2018](#)). Biases in small samples, as well as large distance uncertainties, may contribute to the appearance/disappearance of the chemical discontinuity in the bulge. It is difficult, however, to invoke a bias in the APOGEE inner-Galaxy sample (comprised of many thousands of stars) that would artificially increase the chemical discontinuity.

Figure 7 shows the $[\alpha/\text{Fe}]$ versus $[\text{Fe}/\text{H}]$ plane for the outermost bins in R_{Gal} (the bin 10–12 kpc is repeated from previous figure because the colour scale is slightly different from Fig. 6). Again we observe that for the more distant stars, the addition of the PanSTARRS-1 photometry improves the extinction estimates (compare uncertainty distributions in the top row of the figure). The diagram also clearly confirms the almost total disappearance of the high- $[\alpha/\text{Fe}]$ sequence around ~ 14 kpc. Because the number of stars is small in the very outer disc, the noise in those plots increases, giving more visual weight to outliers.

Finally, we note two other important characteristics of the new maps presented both in Figs. 6 and 7, when focussing on stars near to the Galactic mid-plane ($|Z_{\text{Gal}}| < 0.5$ kpc). Firstly, the $[\alpha/\text{Fe}]$ centroid of the low- $[\alpha/\text{Fe}]$ distribution gradually shifts to larger values with increasing galactocentric distance (especially visible in Fig. 7), corresponding to a positive radial $[\alpha/\text{Fe}]$ gradient, continuing the trend observed at larger galactocentric

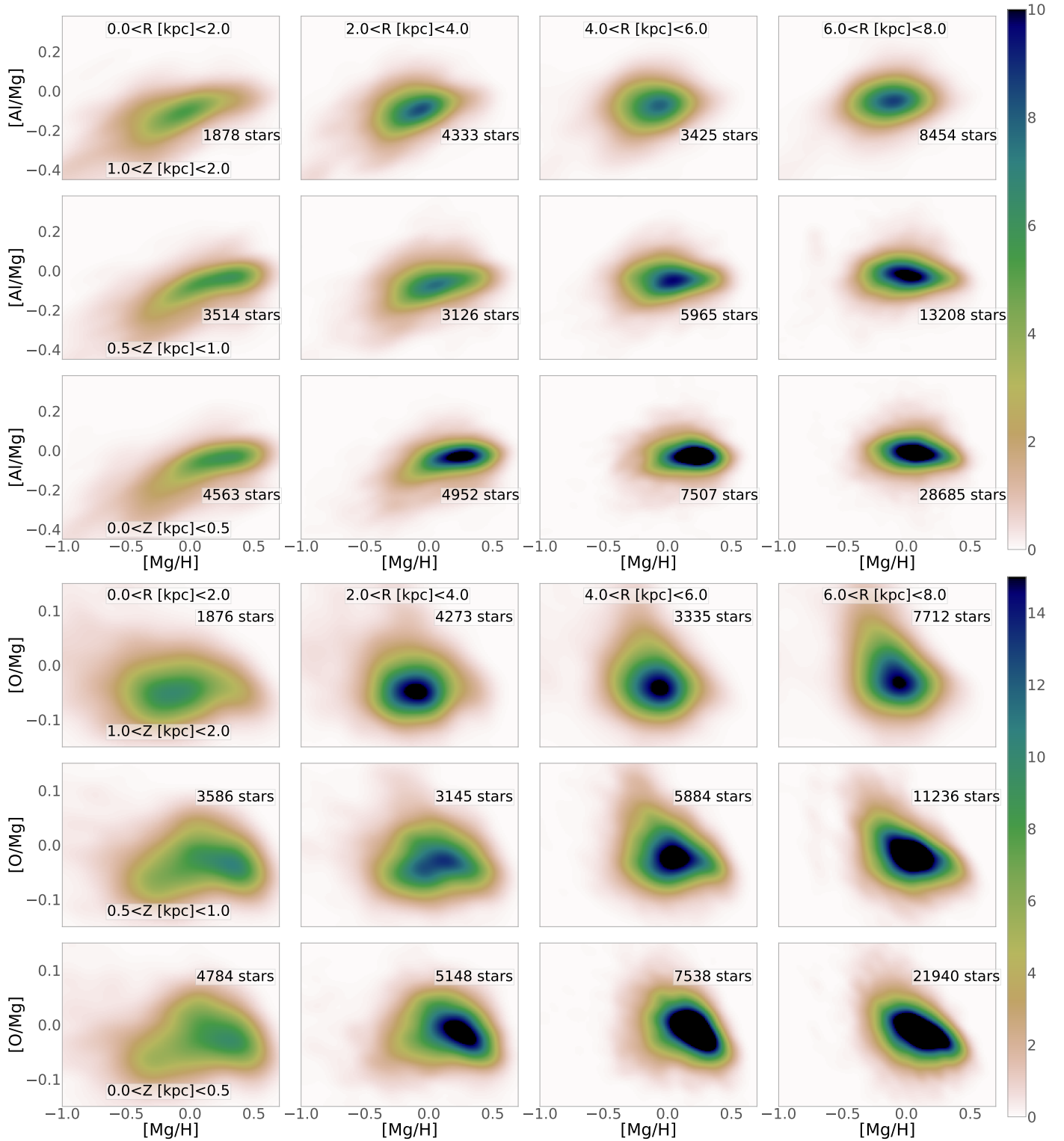


Fig. 9. *Top panel:* APOGEE DR16 [Al/Mg] vs. [Mg/H] diagrams in bins of Galactocentric cylindrical coordinates, similar to Fig. 6, but only out to $R_{\text{Gal}} = 8$ kpc. *Bottom panel:* same for [O/Mg] vs. [Mg/H].

distances (Anders et al. 2014; Hayden et al. 2014). Secondly, in the innermost bin ($R_{\text{Gal}} < 2$ kpc, and $|Z_{\text{Gal}}| < 0.5$ kpc) the $[\alpha/\text{Fe}]$ trend for the more metal-rich, low- $[\alpha/\text{Fe}]$ population ($\sim -0.2 < [\text{Fe}/\text{H}] < 0.5$) is linearly decreasing, without any flattening at larger metallicities. This is in agreement with optical studies of the bulge (Friaça & Barbuy 2017; da Silveira et al. 2018 – see also Barbuy et al. 2018), but remains in stark contrast

to what is observed at larger galactocentric distances (see radial bins from $6 < R_{\text{Gal}} < 12$ kpc, in the same row – $|Z_{\text{Gal}}| < 0.5$ kpc), where the cloud of data bends, thereby showing a flattening of the abundance-ratio trend beyond solar metallicities. The reason for this bending is the migration of old metal-rich stars from the innermost bins towards the outer regions, populating mostly the 8–12 kpc bins.

Indeed, the high-metallicity thin disc stars in the outer regions are known to be migrated stars from the inner disc (e.g. Grenon 1989; Casagrande et al. 2011; Anders et al. 2017a). For example, according to the chemo-dynamical model of Minchev et al. (2013, 2014), the mixture of migrating stars from other galactocentric distances changes when moving from the inner to the outer disc, and even in the 8–12 kpc range there is a large number of migrators from the innermost disc regions. A large number of old inner disc stars can be found around the solar vicinity, according to the predictions of Minchev et al. (2014). This can also be clearly seen in Anders et al. (2017b, their Fig. 1).

The larger statistics of the current maps, especially near the Galactic mid-plane, do not support the dichotomy between the inner and outer discs advertised by Haywood et al. (2019). This suggests instead an inside-out formation of the thin disc, a continuous variation in the chemical properties from the innermost regions towards the outer parts, and significant radial migration (e.g. Frankel et al. 2018).

At larger $|Z_{\text{Gal}}|$ bins and in the outer disc, the combined effects of radial migration and disc flaring make interpretations more complex, and the multif-element abundance maps available from APOGEE offer a unique opportunity to finally quantify all these processes (see e.g. Frankel et al. 2018, 2020 for first attempts on constraining radial migration efficiency using APOGEE red-clump giants with statistical age estimates). In the innermost bins, going from low to large $|Z_{\text{Gal}}|$, we also see a smooth transition from a thin disc-like component to an old (i.e. $[\alpha/\text{Fe}]$ -enhanced) thick disc-like (or spheroidal) component.

Detailed future investigations should use forward simulations to properly take into account selection effects (see e.g. Miranda et al. 2014; Anders et al. 2016; Nandakumar et al. 2017; Fragkoudi et al. 2018; Frankel et al. 2019, for discussions). Moreover, the addition of age and kinematical information is also necessary to be able to disentangle the factors playing a role in these maps, namely, radial migration, population mixture, flaring, and details of the nucleosynthetic yields. An illustrative example is provided by the birth-radius estimation technique proposed by Minchev et al. (2018).

5.2. $[\text{Al}/\text{Fe}]$ versus $[\text{Fe}/\text{H}]$ diagram

Figure 8 shows the same type of plot as Fig. 6, but in this case for the $[\text{Al}/\text{Fe}]$ abundance ratio instead of $[\alpha/\text{Fe}]$. As an additional constraint, we only include stars with well-determined ASPCAP Al abundances ($\text{AL_FE_FLAG}=0$) in this plot. The maps are similar to those in Fig. 6, indicating that overall, Al (being an odd- Z element) behaves like an α element at disc-like metallicities; this was also previously shown to be the case in the bulge (for instance, see discussion in McWilliam 2016). The important difference of Fig. 8 with respect to the corresponding Fig. 6 is the almost complete absence of the bimodality in the abundance plane for galactocentric distances $R_{\text{Gal}} > 2$ kpc.

However, the $[\alpha/\text{Fe}]$ versus $[\text{Fe}/\text{H}]$ discontinuity seen in the very inner regions discussed above is also seen in the $[\text{Al}/\text{Fe}]$ versus $[\text{Fe}/\text{H}]$ diagram: in the $R_{\text{Gal}} < 2$ kpc bin close to the Galactic plane we see essentially two detached $[\text{Al}/\text{Fe}]$ sequences. This fact provides further evidence for the reality of the chemical discontinuity seen in the heart of the Galactic bulge.

The difference between $[\alpha/\text{Fe}]$ and $[\text{Al}/\text{Fe}]$ for the most metal-poor stars is that, whereas the $[\alpha/\text{Fe}]$ seems to continue raising towards lower metallicities, the $[\text{Al}/\text{Fe}]$ starts to bend down. This is a consequence of the metallicity-dependent Al yields in massive stars.

5.3. $[\text{Al}/\text{Mg}]$ versus $[\text{Mg}/\text{H}]$ and $[\text{Mg}/\text{O}]$ versus $[\text{Mg}/\text{H}]$ diagrams

As an example illustrating the wealth of new chemical-abundance information contained in DR16, we now discuss the behaviour of the ratios between two α -like elements that use magnesium rather than iron as a reference element. Because Mg is mainly a product of core collapse supernovae, its increase with time follows the star formation rate more closely than iron, which can keep increasing even if the star formation stops as a result of the contribution of type Ia supernovae released on longer timescales. From the observational side, magnesium is also a convenient element because the calibrated ASPCAP $[\text{Mg}/\text{H}]$ abundances show small dispersions, very small trends with effective temperature, and they follow the expected trends in the abundance diagrams.

Figure 9 shows both an $[\text{Al}/\text{Mg}]$ versus $[\text{Mg}/\text{H}]$ and an $[\text{O}/\text{Mg}]$ versus $[\text{Mg}/\text{H}]$ map of the Galaxy, focussing on the inner disc and bulge region ($R_{\text{Gal}} < 8$ kpc). In both plots, we again only plot stars with high-quality DR16 ASPCAP abundances, by requiring the corresponding abundance flag entries (MG_FE_FLAG and, respectively, AL_FE_FLAG and O_FE_FLAG) to equal zero.

The main point of Fig. 9 is to showcase the vast amount of new high-quality APOGEE data, especially for the inner disc. To appreciate the increase of the sample with respect to DR14, Fig. 9 should be compared to Figs. 4 and 5 of Weinberg et al. (2019), which was based on a small sample of 20 000 stars with only slightly stricter quality requirements ($3700 \text{ K} < T_{\text{eff}} < 4600 \text{ K}$, $\text{SNREV} > 80$, no “ASPCAP bad” flags, $\text{EXTRATARG}=0$). The new data clearly allow us to study the very heart of our Galaxy in much more detail, even when the same quality cuts are applied.

The main isotopes of both O and Mg are produced during the hydrostatic phases of high-mass stars. This ratio is then mostly sensitive to details of related to the stellar yields, such as mass loss and rotation in the case of oxygen and convection treatment in the case of Mg, but is expected to remain close to solar (Woosley et al. 2002; Sukhbold et al. 2016; Groh et al. 2019).

The following two things can be noted in the $[\text{O}/\text{Mg}]$ versus $[\text{Mg}/\text{H}]$ diagrams in the inner Galaxy (Fig. 9): a systematic slight increase of the $[\text{O}/\text{Mg}]$ median value from the innermost regions towards the solar neighbourhood for stars in the top row ($1 \text{ kpc} < |Z_{\text{Gal}}| < 2 \text{ kpc}$) and a less pronounced presence of the low- $[\text{Mg}/\text{H}]$ low- $[\text{O}/\text{Mg}]$ population towards the mid-plane that remains visible only in the innermost bin.

In order to understand if this is due to O or Mg, we next checked the $[\text{Al}/\text{Mg}]$ diagrams (bottom panel of Fig. 9). Similarly, the median $[\text{Al}/\text{Mg}]$ ratio in the top row ($1 \text{ kpc} < |Z_{\text{Gal}}| < 2 \text{ kpc}$) increases with galactocentric distance, reaching the solar value at the solar ring. Moreover, $[\text{Al}/\text{Mg}]$ also increases with metallicity in the smallest galactocentric distance bins.

Taking both results at face value, without considering further biases that could be affecting proportions of stars in the different loci of these diagrams, the results suggest that there is an increase of Mg towards larger metallicities or a relative decrease of both O and Al (e.g. Groh et al. 2019).

6. StarHorse results for other publicly released spectroscopic surveys

In this paper we also provide distances and extinctions for different spectroscopic surveys, namely for GALAH DR2

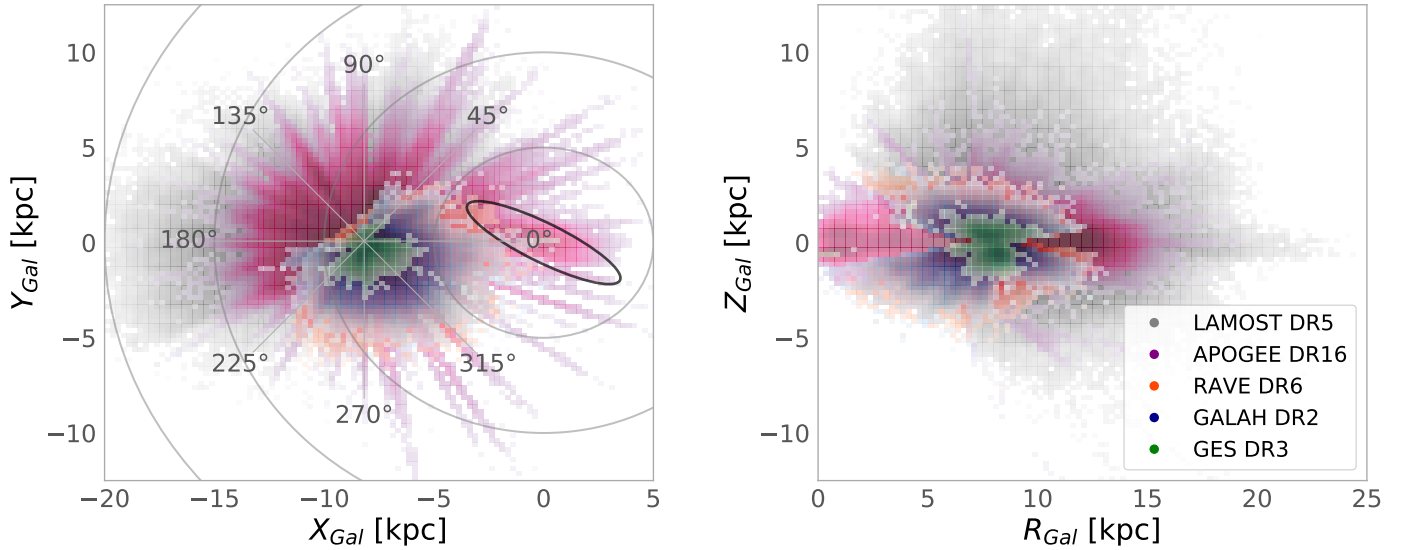


Fig. 10. Survey coverage of the catalogues presented in this paper in galactocentric coordinates. In both panels, the colours indicate the different surveys (grey: LAMOST DR5; magenta: APOGEE DR16; red: RAVE DR6; blue: GALAH DR2; and green: GES DR3) and the relative density of observed stars (bins with less than five stars are left blank). To guide the eye, grey circles are placed in multiples of 5 kpc around the Galactic centre, the expected location of the Galactic bar (e.g. [Bland-Hawthorn & Gerhard 2016](#)) is indicated by the black ellipse, and a heliocentric Galactic longitude frame is over-plotted. *Left panel:* Cartesian XY coordinates. *Right panel:* cylindrical RZ coordinates.

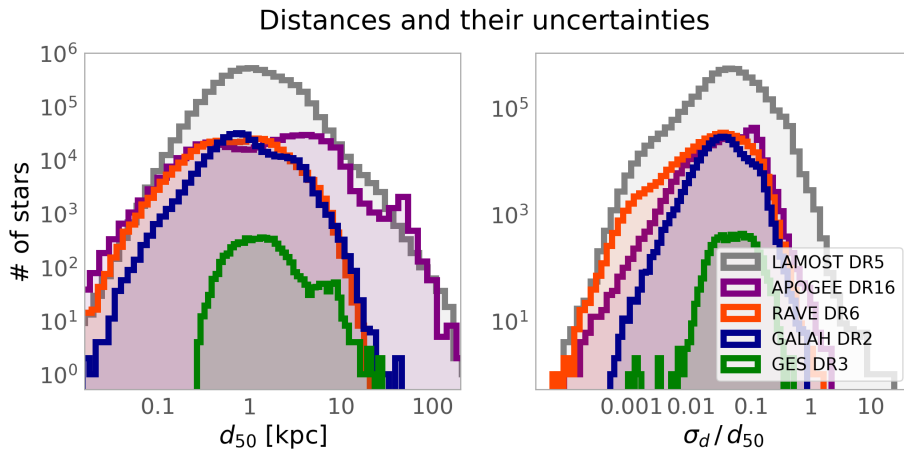


Fig. 11. Distribution of posterior distances (*left*) and their corresponding relative uncertainties (*right*) for the catalogues presented in this paper. In both panels, the axes are logarithmic and the colours are the same as in Fig. 10 (grey: LAMOST DR5, magenta: APOGEE DR16, red: RAVE DR6, blue: GALAH DR2, and green: GES DR3).

([Buder et al. 2018](#)), LAMOST DR5 ([Xiang et al. 2019](#)), RAVE DR6 ([Steinmetz et al. 2020a](#)), and GES DR3 ([Gilmore 2012](#)). We again used *Gaia* DR2 parallaxes ([Gaia Collaboration 2018](#)). Moreover, we also included photometry from APASS ([Henden & Munari 2014](#)) that was not included in the APOGEE run. Also, since none of these surveys extend to the very extinguished regions, we used *Gaia* DR2 photometry in this case.

Gaia contains three passbands G , G_{BP} , and G_{RP} in the respective wavelengths 320–1050 nm, 320–680 nm, and 610–1070 nm ([Gaia Collaboration 2016](#); [Weiler 2018](#)). Even though this photometry is very precise, there are some discrepancies between observations and the sensitivity curves published. To correct for this effect, we followed the recommendations of [Maíz Apellániz & Weiler \(2018\)](#); these are the same corrections as applied in [Anders et al. \(2019, see their Table 1\)](#).

We computed distances and extinctions in the same way as for APOGEE DR16, for which we present catalogues in the same format as before (Table A.1). Figure 10 shows the resulting spatial coverage of the surveys analysed in this work, and Fig. 11 shows the corresponding distance and distance uncertainty dis-

tributions. In addition, in Appendix C we provide summary plots similar to Figs. 2, 3, and 1, demonstrating the sky coverage and the quality of the results for each of the surveys. In the following subsections we describe the assumptions made in each of these catalogues.

6.1. GALAH DR2

The spectroscopic survey GALAH ([De Silva et al. 2015](#); [Martell et al. 2017](#)) aims to identify stellar groups that were born together, by searching for similarity on the chemical patterns of the stars. Therefore GALAH spectra were obtained with the high-resolution and multi-band spectrograph HERMES ([Barden et al. 2010](#)), which is capable to deliver abundances for up to 23 chemical elements. Its latest data release, GALAH DR2 release in April 2018, contains radial velocities, atmospheric parameters, and abundances for a total of 342 682 unique stars ([Buder et al. 2018](#)).

The GALAH survey maps all stellar populations between magnitudes ($12 < V < 14$) and avoids the Galactic plane

$|b| > 10$. In Q18 we computed distances and extinctions using the GALAH DR1 parameters combined with *Gaia* DR1. Now we have available much more data both in GALAH DR2 and *Gaia* DR2. We followed the same procedure in this work as in Q18 to run this latest public GALAH data. The atmospheric parameters were treated as they come in the catalogue. We again used the (Salaris et al. 1993) correction for stars that have $[\alpha/\text{Fe}]$ (see Sect. 3.1). For those without a reported $[\alpha/\text{Fe}]$ ratio, we assumed $[\text{M}/\text{H}] = [\text{Fe}/\text{H}]$.

We chose to run GALAH with APASS photometry since its faint limits are still too bright to be able to use PanSTARRS-1 (due to saturation). We also ran StarHorse with parallax True mode (see Q18 Sect. 3.2.1) since more than 90% of the catalogue contains parallaxes uncertainties better than 20%. From the input catalogue a total of 324 999 stars converged (94%) with solutions of distances, extinctions, and astrophysical parameters that can be downloaded via the CDS.

6.2. LAMOST DR5 DD-Payne VAC

The survey LAMOST (Cui et al. 2012; Zhao et al. 2012) is one of the largest scale spectroscopic surveys and the first large astronomical device in China. This instrument has been collecting data since 2012, and now after about eight years the survey has released nine million spectra in the wavelength range of 3690–9100 Å and spectral resolution of $R \sim 1800$. These nine million spectra contain stars, galaxies, quasars, and non-classified sources.

We adopted the recently published DR5 DD-Payne VAC⁵ (Xiang et al. 2019) catalogue. This catalogue contains stellar parameters and individual elemental abundances for six million LAMOST DR5 stars, obtained with a data-driven approach incorporating constraints from theoretical spectra and trained on GALAH DR2 and APOGEE DR14 results.

From this catalogue we only selected stars with stellar parameters with uncertainties in gravity, surface temperature, metallicity, and $[\alpha/\text{Fe}]$ ratios smaller than $\sigma_{\log g} < 1$ dex, $\sigma_{T_{\text{eff}}} < 800$ K, $\sigma_{[\text{Fe}/\text{H}]} < 1.0$ dex, and $\sigma_{[\alpha/\text{Fe}]} < 1.0$, respectively. The goal was to avoid stars with too large uncertainties and save computing time.

For LAMOST DR5 we combined the spectra again with *Gaia* parallaxes and photometry. We complemented the input data with photometry from PanSTARRS1, 2MASS, and WISE. We also ran LAMOST with parallax true mode since most parallaxes in LAMOST also have uncertainties better than 20%. From 5 651 710 sources with available parallaxes StarHorse converged for 4 928 715 stars (87%). One of the reasons for a smaller convergence in the case of LAMOST is the fact that we used a thicker spaced PARSEC model grid (0.05 Gyr in age and 0.05 dex in $[\text{M}/\text{H}]$). The solutions of distances, extinctions, and astrophysical parameters can be downloaded via the CDS.

6.3. RAVE DR6

We obtained the RAVE spectra with the multi-object spectrograph deployed on 1.2 m UK Schmidt Telescope of the Australian Astronomical Observatory (AAO). The spectra have a medium resolution of ($R \sim 7500$) and cover the CaII-triplet region (8410–8795 Å). We used the final RAVE data release, DR6 (Steinmetz et al. 2020a), and in particular, the purely spectroscopically derived stellar atmospheric parameters subscripted `cal_madera` (Steinmetz et al. 2020b). The uncertainties that we

use are, in general, the maximum between the calibrated and not calibrated parameters given in the catalogue or a fiducial maximum. These corrections are very similar to those applied to run RAVE DR5 combined with *Gaia* DR1 in Q18. We then combined RAVE DR6 with *Gaia* DR2 parallaxes and the photometric data used in this case is the same as for LAMOST. We configured StarHorse to use the `parallax=true` option and the same coarser isochrone grid we used for LAMOST, since the uncertainties of these surveys are larger. From the input catalogue of DR6 (488 233 unique objects), 408 894 stars converged, and we make their derived astrophysical stellar parameters available in this work. Because of the significantly smaller formal uncertainties of the DR6 MADERA stellar parameters compared to DR5, the number of stars for which StarHorse converged is slightly smaller than for DR5.

6.4. GES survey DR3

The large public spectroscopic survey GES (Gilmore 2012) has a high resolution that covers all Milky Way components and open star clusters of all ages and masses. The final GES release is expected to include about 10^5 stars. We downloaded the GES Data Release 3 (DR3) from the ESO catalogue facility. This catalogue contains a total of 25 533 stars, including the Milky Way field, open clusters, and calibration stars. We selected only the stars in the Milky Way field to produce our StarHorse, which is about 7870 stars. In this case we also made a quality criteria cut, that is, $\sigma_{\log g} < 0.4$ dex, $\sigma_{T_{\text{eff}}}/T_{\text{eff}} < 0.05$ K, $\sigma_{[\text{Fe}/\text{H}]} < 0.2$ dex. The final catalogue used as StarHorse input contains then 6316 stars. The complementary photometric data used in this case is the same as for LAMOST. We then ran the code again with parallax True mode, and StarHorse converged for 6095 stars. The StarHorse astrophysical parameters for the GES DR3 stars are also at the CDS.

7. Conclusions

With this paper we present a set of VACs derived from the stellar spectroscopic surveys APOGEE, GALAH, LAMOST, RAVE, and GES. In particular our APOGEE DR16 VAC, released as part of SDSS DR16 (SDSS-IV Collaboration 2019), was produced by running the StarHorse code, which is described in detail by Q18, in the DR16 ASPCAP catalogue matched to *Gaia* DR2 with the addition of photometry from PanSTARRS-1, 2MASS, and AllWISE. This VAC contains distance and extinction estimates for 388 815 unique stars out of a total of 437 485 unique objects contained in the DR16 catalogue. Our code was validated extensively in Santiago et al. (2016), Queiroz et al. (2018), and Anders et al. (2019). In Appendix B we provide some additional tests showing that the newly derived parameters for APOGEE DR16 generally compare well to results obtained from asteroseismology, open clusters, and other spectroscopic surveys. There is evidence for slightly overestimated extinctions for our APOGEE DR16 VAC, which we attribute in part to the missing reliable optical photometry for most of this sample, and in part to an offset in the ASPCAP temperature scale, especially outside the recommended calibration regime.

In Appendix B we also show that our distances are less biased towards the inner Galactic disc than the neural-network based distances of Leung & Bovy (2019) (see Fig. B.6). The typical uncertainties for the APOGEE DR16 sample are of the order of $\approx 10\%$ in distance and of 0.16 mag in A_V . A clearly bimodal distribution of extinction uncertainties is observed with the peak at $\sigma_{A_V} \approx 0.06$ found for stars with available optical magnitudes

⁵ <http://dr5.lamost.org/doc/vac>

from PanSTARRS-1, while the peak at larger σ_{A_V} is made by stars with no such measurements. The typical distance uncertainties are also different for dwarfs ($\approx 2\%$) and giants ($\approx 5\%$). The scientific results from the first analysis of the StarHorse APOGEE DR16 catalogue can be summarised as

- Using the StarHorse VAC we demonstrate that the APOGEE DR16 sample represents a major leap in terms of coverage of the Galactic disc with high-resolution spectra. The density of APOGEE targets exceeds a dozen stars per kiloparsec² everywhere in the $R_{\text{Gal}}-Z_{\text{Gal}}$ plane for $0 < R_{\text{Gal}} < 18$ kpc and -3 kpc $< Z_{\text{Gal}} < 3$ pc, allowing for an unprecedented chemo-kinematic mapping of the inner and outer stellar discs with significant azimuthal coverage.
- From the improved APOGEE coverage and StarHorse distances we can see a bar signature in the density maps projected in XY Galactocentric coordinates; this is also found in A19. However the bar signature found in this work has a smaller angle with respect to the Galactic plane, which is more consistent with previous studies about the Galactic bar structure (Bland-Hawthorn & Gerhard 2016).
- The extended chemical-abundance maps in Fig. 6 confirms, for the first time with good statistics of thousands of stars, a chemical bimodality in the very inner Galaxy $0 < R_{\text{Gal}} < 2$ kpc and $0 < |Z_{\text{Gal}}| < 1$ kpc. This is different from previous analyses that reported a single sequence (Hayden et al. 2015; Zasowski et al. 2019), but with much less populated samples.
- The two groups visible in the $[\alpha/\text{Fe}]-[\text{Fe}/\text{H}]$ plane in the innermost bin completely define the detached sequences, implying a true chemical discontinuity. The larger statistics of the current maps, especially near the Galactic mid-plane, do not support the dichotomy between the inner and outer discs. On the other hand, it suggests the chemical discontinuity to be a clear property of the global chemical-enrichment history of the Milky Way.
- The chemical maps of $[\alpha/\text{Fe}]-[\text{Fe}/\text{H}]$ extend to the very outer disc, $R_{\text{Gal}} > 20$ kpc, and also show the complete disappearance of a high-alpha population further than $R_{\text{Gal}} > 14$ kpc. This confirms the shorter scale length of the Galactic thick disc concerning the Galactic thin disc, following previous studies (Cheng et al. 2012; Anders et al. 2014).
- There is an indication for a positive radial $[\alpha/\text{Fe}]$ gradient, observed from the fact that the $[\alpha/\text{Fe}]$ centroid of the α -poor sequence in the inner Galaxy gradually shifts to larger values with increasing Galactocentric radius observed in Figs. 6 and 7 continuing the trend reported by Anders et al. (2014), and Hayden et al. (2014).
- The maps of $[\alpha/\text{Fe}]$ show some evidence for radial migration of old metal-rich stars from the inner Galaxy to the outer Galaxy; this is shown by the flattening of the abundance-ratio trend beyond the solar metallicities.
- The chemical duality in the inner bins is also confirmed in maps using aluminium and iron, $[\text{Al}/\text{Fe}]-[\text{Fe}/\text{H}]$. This is not seen for larger Galactocentric distances, where the disc chemical bimodality disappears in this abundance regime. This indicates a strong chemical duality in the inner Galaxy. Those diagrams also show metallicity-dependent Al yields in massive stars, with $[\text{Al}/\text{Fe}]$ starting to bend down towards lower metallicities.
- The resulting maps using α -elements and magnesium as a reference instead of iron, show an increase of Mg with respect to Galactocentric distance. Since Mg follows the star formation more closely than iron, this suggests an inside-out formation.

The data produced in this work and made publicly available allow for much more sophisticated chemical-abundance studies over much larger disc volumes than previous data releases. New studies also gathering kinematic information will enable unprecedented constraints for chemo-dynamical models of the Milky Way, especially in the inner-most and outer-most Galaxy.

All the newly produced StarHorse catalogues are available for download online⁶ please use the DOI to quote the data: DOI:10.17876/data/2020_2.

Acknowledgements. The StarHorse code is written in python 3.6 and makes use of several community-developed python packages, among them *astropy* (Astropy Collaboration 2013), *ezpadova* (<https://github.com/mfouesneau/ezpadova>), *numpy* and *scipy* (Virtanen et al. 2020), and *matplotlib* (Hunter 2007). The code also makes use of the photometric filter database of VOSA (Bayo et al. 2008), developed under the Spanish Virtual Observatory project supported from the Spanish MICINN through grant AyA2011-24052. Funding for the SDSS Brazilian Participation Group has been provided by the Ministério de Ciência e Tecnologia (MCT), Fundação Carlos Chagas Filho de Amparo à Pesquisa do Estado do Rio de Janeiro (FAPERJ), Conselho Nacional de Desenvolvimento Científico e Tecnológico (CNPq), and Financiadora de Estudos e Projetos (FINEP). Funding for the Sloan Digital Sky Survey IV has been provided by the Alfred P. Sloan Foundation, the US Department of Energy Office of Science, and the Participating Institutions. SDSS-IV acknowledges support and resources from the Center for High-Performance Computing at the University of Utah. The SDSS web site is www.sdss.org. SDSS-IV is managed by the Astrophysical Research Consortium for the Participating Institutions of the SDSS Collaboration including the Brazilian Participation Group, the Carnegie Institution for Science, Carnegie Mellon University, the Chilean Participation Group, the French Participation Group, Harvard-Smithsonian Center for Astrophysics, Instituto de Astrofísica de Canarias, The Johns Hopkins University, Kavli Institute for the Physics and Mathematics of the Universe (IPMU)/University of Tokyo, Lawrence Berkeley National Laboratory, Leibniz-Institut für Astrophysik Potsdam (AIP), Max-Planck-Institut für Astronomie (MPIA Heidelberg), Max-Planck-Institut für Astrophysik (MPA Garching), Max-Planck-Institut für Extraterrestrische Physik (MPE), National Astronomical Observatory of China, New Mexico State University, New York University, University of Notre Dame, Observatório Nacional/MCTI, The Ohio State University, Pennsylvania State University, Shanghai Astronomical Observatory, United Kingdom Participation Group, Universidad Nacional Autónoma de México, University of Arizona, University of Colorado Boulder, University of Oxford, University of Portsmouth, University of Utah, University of Virginia, University of Washington, University of Wisconsin, Vanderbilt University, and Yale University. Guoshoujing Telescope (the Large Sky Area Multi-Object Fiber Spectroscopic Telescope LAMOST) is a National Major Scientific Project built by the Chinese Academy of Sciences. Funding for the project has been provided by the National Development and Reform Commission. LAMOST is operated and managed by the National Astronomical Observatories, Chinese Academy of Sciences. Funding for RAVE has been provided by: the Australian Astronomical Observatory; the Leibniz-Institut für Astrophysik Potsdam (AIP); the Australian National University; the Australian Research Council; the French National Research Agency; the German Research Foundation (SPP 1177 and SFB 881); the European Research Council (ERC-StG 240271 Galactica); the Istituto Nazionale di Astrofisica at Padova; The Johns Hopkins University; the National Science Foundation of the USA (AST-0908326); the W. M. Keck foundation; the Macquarie University; the Netherlands Research School for Astronomy; the Natural Sciences and Engineering Research Council of Canada; the Slovenian Research Agency; the Swiss National Science Foundation; the Science & Technology Facilities Council of the UK; Opticon; Strasbourg Observatory; and the Universities of Groningen, Heidelberg and Sydney. The RAVE web site is at <https://www.rave-survey.org>. This work has made use of data from the European Space Agency (ESA) mission *Gaia* (<http://www.cosmos.esa.int/gaia>), processed by the *Gaia* Data Processing and Analysis Consortium (DPAC, <http://www.cosmos.esa.int/web/gaia/dpac/consortium>). Funding for the DPAC has been provided by national institutions, in particular the institutions participating in the *Gaia* Multilateral Agreement. This work has also made use of data from *Gaia*-ESO based on data products from observations made with ESO Telescopes at the La Silla Paranal Observatory under programme ID 188.B-3002. FA is grateful for funding from the European Union's Horizon 2020 research and innovation programme under the Marie Skłodowska-Curie grant agreement No. 800502 H2020-MSCA-IF-EF-2017. CC acknowledges support from DFG Grant CH1188/2-1 and from the ChETEC COST Action (CA16117), supported by

⁶ <https://data.aip.de/aqueiroz2020>

COST (European Cooperation in Science and Technology). DAGH acknowledges support from the State Research Agency (AEI) of the Spanish Ministry of Science, Innovation and Universities (MCIU) and the European Regional Development Fund (FEDER) under grant AYA2017-88254-P. J.G.F.-T. is supported by FONDECYT No. 3180210. DB is supported in the form of work contract FCT/MCTES through national funds and by FEDER through COMPETE2020 in connection to these grants: UID/FIS/04434/2019; PTDC/FIS-AST/30389/2017 & POCI-01-0145-FEDER-030389. AB thanks Cosmos.

References

- Abolfathi, B., Aguado, D. S., Aguilar, G., et al. 2018, *ApJS*, **235**, 42
- Alam, S., Albareti, F. D., Allende Prieto, C., Anders, F., & Anderson, S. F. 2015, *ApJS*, **219**, 12
- Allende Prieto, C., Majewski, S. R., Schiavon, R., et al. 2008, *Astron. Nachr.*, **329**, 1018
- Alves-Brito, A., Meléndez, J., Asplund, M., Ramírez, I., & Yong, D. 2010, *A&A*, **513**, A35
- Anders, F., Chiappini, C., Santiago, B. X., et al. 2014, *A&A*, **564**, A115
- Anders, F., Chiappini, C., Rodrigues, T. S., et al. 2016, *Astron. Nachr.*, **337**, 926
- Anders, F., Chiappini, C., Rodrigues, T. S., et al. 2017a, *A&A*, **597**, A30
- Anders, F., Chiappini, C., Minchev, I., et al. 2017b, *A&A*, **600**, A70
- Anders, F., Chiappini, C., Santiago, B. X., et al. 2018, *A&A*, **619**, A125
- Anders, F., Khalatyan, A., Chiappini, C., et al. 2019, *A&A*, **628**, A94
- Andrae, R., Fouesneau, M., Creevey, O., et al. 2018, *A&A*, **616**, A8
- Arenou, F., Luri, X., Babusiaux, C., et al. 2018, *A&A*, **616**, A17
- Astropy Collaboration (Robitaille, T. P., et al.) 2013, *A&A*, **558**, A33
- Baglin, A., Auvergne, M., Barge, P., et al. 2006, in *ESA SP*, eds. M. Fridlund, A. Baglin, J. Lochard, & L. Conroy, 1306, 33
- Barbuy, B., Chiappini, C., & Gerhard, O. 2018, *ARA&A*, **56**, 223
- Barden, S. C., Jones, D. J., Barnes, S. I., et al. 2010, in *SPIE Conf. Ser.*, Proc. SPIE, **7735**, 773509
- Bayo, A., Rodrigo, C., Barrado Y Navascués, D., et al. 2008, *A&A*, **492**, 277
- Bensby, T., Alves-Brito, A., Oey, M. S., Yong, D., & Meléndez, J. 2010, *A&A*, **516**, L13
- Bensby, T., Alves-Brito, A., Oey, M. S., Yong, D., & Meléndez, J. 2011, *ApJ*, **735**, L46
- Bensby, T., Feltzing, S., Gould, A., et al. 2017, *A&A*, **605**, A89
- Binney, J., Burnett, B., Kordopatis, G., et al. 2014, *MNRAS*, **437**, 351
- Bland-Hawthorn, J., & Gerhard, O. 2016, *ARA&A*, **54**, 529
- Blanton, M. R., Bershady, M. A., Abolfathi, B., et al. 2017, *AJ*, **154**, 28
- Bossini, D., Vallenari, A., Bragaglia, A., et al. 2019, *A&A*, **623**, A108
- Bovy, J., & Rix, H.-W. 2013, *ApJ*, **779**, 115
- Bovy, J., Leung, H. W., Hunt, J. A. S., et al. 2019, *MNRAS*, **490**, 4740
- Bowen, I. S., & Vaughan, A. H. J. 1973, *Appl. Opt.*, **12**, 1430
- Bressan, A., Marigo, P., Girardi, L., et al. 2012, *MNRAS*, **427**, 127
- Buck, T. 2020, *MNRAS*, **491**, 5435
- Buder, S., Asplund, M., Duong, L., et al. 2018, *MNRAS*, **478**, 4513
- Burnett, B., & Binney, J. 2010, *MNRAS*, **407**, 339
- Burnett, B., Binney, J., Sharma, S., et al. 2011, *A&A*, **532**, A113
- Cantat-Gaudin, T., Jordi, C., Vallenari, A., et al. 2018, *A&A*, **618**, A93
- Carrillo, I., Minchev, I., Steinmetz, M., et al. 2019, *MNRAS*, **490**, 797
- Casagrande, L., Schönrich, R., Asplund, M., et al. 2011, *A&A*, **530**, A138
- Chabrier, G. 2003, *PASP*, **115**, 763
- Chambers, K. C., Magnier, E. A., Metcalfe, N., et al. 2016, ArXiv e-prints [arXiv:1612.05560]
- Cheng, J. Y., Rockosi, C. M., Morrison, H. L., et al. 2012, *ApJ*, **752**, 51
- Chiappini, C., Matteucci, F., & Gratton, R. 1997, *ApJ*, **477**, 765
- Cui, X.-Q., Zhao, Y.-H., Chu, Y.-Q., et al. 2012, *Res. Astron. Astrophys.*, **12**, 1197
- Cutri, R. M., Skrutskie, M. F., & van Dyk, S. 2003, *The IRSA 2MASS All-Sky Point Source Catalog, NASA/IPAC Infrared Science Archive*
- Cutri, R. M., Wright, E. L., Conrow, T., et al. 2013, *Explanatory Supplement to the AllWISE Data Release Products*, Tech. rep.
- da Silva, C. R., Barbuy, B., Friaça, A. C. S., et al. 2018, *A&A*, **614**, A149
- De Silva, G. M., Freeman, K. C., Bland-Hawthorn, J., et al. 2015, *MNRAS*, **449**, 2604
- Eisenstein, D. J., Weinberg, D. H., Agol, E., et al. 2011, *AJ*, **142**, 72
- Elyajouri, M., & Lallement, R. 2019, *A&A*, **628**, A67
- Evans, D. W., Riello, M., De Angeli, F., et al. 2018, *A&A*, **616**, A4
- Fernández-Alvar, E., Carigi, L., Allende Prieto, C., et al. 2017, *MNRAS*, **465**, 1586
- Fernández-Alvar, E., Carigi, L., Schuster, W. J., et al. 2018, *ApJ*, **852**, 50
- Fernández-Trincado, J. G., Beers, T. C., Placco, V. M., et al. 2019, *ApJ*, **886**, L8
- Fragkoudi, F., Di Matteo, P., Haywood, M., et al. 2018, *A&A*, **616**, A180
- Frankel, N., Rix, H.-W., Ting, Y.-S., Ness, M., & Hogg, D. W. 2018, *ApJ*, **865**, 96
- Frankel, N., Sanders, J., Rix, H.-W., Ting, Y.-S., & Ness, M. 2019, *ApJ*, **884**, 99
- Frankel, N., Sanders, J., Ting, Y. S., & Rix, H. W. 2020, *ApJ*, submitted [arXiv:2002.04622]
- Friaça, A. C. S., & Barbuy, B. 2017, *A&A*, **598**, A121
- Fuhrmann, K. 1998, *A&A*, **338**, 161
- Fuhrmann, K. 2011, *MNRAS*, **414**, 2893
- Gaia Collaboration (Prusti, T., et al.) 2016, *A&A*, **595**, A1
- Gaia Collaboration (Brown, A. G. A., et al.) 2018, *A&A*, **616**, A1
- García Pérez, A. E., Allende Prieto, C., Holtzman, J. A., et al. 2016, *AJ*, **151**, 144
- Gilmore, G. 2012, in *Galactic Archaeology: Near-Field Cosmology and the Formation of the Milky Way*, eds. W. Aoki, M. Ishigaki, T. Suda, T. Tsujimoto, & N. Arimoto, *ASP Conf. Ser.*, **458**, 147
- Gilmore, G., Randich, S., Asplund, M., et al. 2012, *The Messenger*, **147**, 25
- Girardi, L., Dalcanton, J., Williams, B., et al. 2008, *PASP*, **120**, 583
- Grenon, M. 1989, *Ap&SS*, **156**, 29
- Grievés, N., Ge, J., Thomas, N., et al. 2018, *MNRAS*, **481**, 3244
- Groh, J. H., Ekström, S., Georgy, C., et al. 2019, *A&A*, **627**, A24
- Gunn, J. E., Siegmund, W. A., Mannery, E. J., et al. 2006, *AJ*, **131**, 2332
- Hayden, M. R., Holtzman, J. A., Bovy, J., et al. 2014, *AJ*, **147**, 116
- Hayden, M. R., Bovy, J., Holtzman, J. A., et al. 2015, *ApJ*, **808**, 132
- Haywood, M., Lehnert, M. D., Di Matteo, P., et al. 2016, *A&A*, **589**, A66
- Haywood, M., Di Matteo, P., Lehnert, M., et al. 2018, *A&A*, **618**, A78
- Haywood, M., Snaith, O., Lehnert, M. D., Di Matteo, P., & Khoperskov, S. 2019, *A&A*, **625**, A105
- Henden, A., & Munari, U. 2014, *Contrib. Astron. Obs. Skalnate Pleso*, **43**, 518
- Holtzman, J. A., Burrows, C. J., Casertano, S., et al. 1995, *PASP*, **107**, 1065
- Hunter, J. D. 2007, *Comput. Sci. Eng.*, **9**, 90
- Jofré, P., Heiter, U., & Soubiran, C. 2019, *ARA&A*, **57**, 571
- Katz, D., Sartoretti, P., Cropper, M., et al. 2019, *A&A*, **622**, A205
- Khan, S., Miglio, A., Mosser, B., et al. 2019, *A&A*, **628**, A35
- Kunder, A., Kordopatis, G., Steinmetz, M., et al. 2017, *AJ*, **153**, 75
- Leung, H. W., & Bovy, J. 2019, *MNRAS*, **483**, 3255
- Lindgren, L., Hernández, J., Bombrun, A., et al. 2018, *A&A*, **616**, A2
- Luri, X., Brown, A. G. A., Sarro, L. M., et al. 2018, *A&A*, **616**, A9
- Mackereth, J. T., Bovy, J., Schiavon, R. P., et al. 2017, *MNRAS*, **471**, 3057
- Mackereth, J. T., Crain, R. A., Schiavon, R. P., et al. 2018, *MNRAS*, **477**, 5072
- Maíz Apellániz, J., & Weiler, M. 2018, *A&A*, **619**, A180
- Majewski, S. R., Schiavon, R. P., Frinchaboy, P. M., et al. 2017, *AJ*, **154**, 94
- Marigo, P., Girardi, L., Bressan, A., et al. 2017, *ApJ*, **835**, 77
- Marrese, P. M., Marinoni, S., Fabrizio, M., & Altavilla, G. 2019, *A&A*, **621**, A144
- Martell, S. L., Sharma, S., Buder, S., et al. 2017, *MNRAS*, **465**, 3203
- Martig, M., Fouesneau, M., Rix, H.-W., et al. 2016, *MNRAS*, **456**, 3655
- Matteucci, F. 2012, *Chemical Evolution of Galaxies* (Berlin, Heidelberg: Springer-Verlag)
- McWilliam, A. 2016, *PASA*, **33**, e040
- Mikolaitis, Š., Hill, V., Recio-Blanco, A., et al. 2014, *A&A*, **572**, A33
- Minchev, I., Chiappini, C., & Martig, M. 2013, *A&A*, **558**, A9
- Minchev, I., Chiappini, C., & Martig, M. 2014, *A&A*, **572**, A92
- Minchev, I., Martig, M., Streich, D., et al. 2015, *ApJ*, **804**, L9
- Minchev, I., Anders, F., Recio-Blanco, A., et al. 2018, *MNRAS*, **481**, 1645
- Minchev, I., Matijević, G., Hogg, D. W., et al. 2019, *MNRAS*, **487**, 3946
- Miranda, M. S., Macfarlane, B. A., & Gibson, B. K. 2014, *Proceedings of XIII Nuclei in the Cosmos (NIC XIII). 7—11 July, 2014. Debrecen, Hungary*, Online at <http://pos.sissa.it/cgi-bin/reader/conf.cgi?confid=204>, 149
- Monaghan, J. J. 1992, *ARA&A*, **30**, 543
- Monari, G., Famaey, B., Carrillo, I., et al. 2018, *A&A*, **616**, L9
- Nandakumar, G., Schultheis, M., Hayden, M., et al. 2017, *A&A*, **606**, A97
- Ness, M. K., Johnston, K. V., Blancato, K., et al. 2019, *ApJ*, **883**, 177
- Nidever, D. L., Bovy, J., Bird, J. C., et al. 2014, *ApJ*, **796**, 38
- Nidever, D. L., Holtzman, J. A., Allende Prieto, C., et al. 2015, *AJ*, **150**, 173
- Nuza, S. E., Scannapieco, C., Chiappini, C., et al. 2019, *MNRAS*, **482**, 3089
- Palicio, P. A., Martínez-Valpuesta, I., Allende Prieto, C., et al. 2018, *MNRAS*, **478**, 1231
- Paxton, B., Bildsten, L., Dotter, A., et al. 2011, *ApJS*, **192**, 3
- Queiroz, A. B. A., Anders, F., Santiago, B. X., et al. 2018, *MNRAS*, **476**, 2556
- Recio-Blanco, A., Rojas-Arriagada, A., de Laverny, P., et al. 2017, *A&A*, **602**, L14
- Riess, A. G., Casertano, S., Yuan, W., et al. 2018, *ApJ*, **861**, 126
- Rodrigues, T. S., Bossini, D., Miglio, A., et al. 2017, *MNRAS*, **467**, 1433
- Rojas-Arriagada, A., Zoccali, M., Schultheis, M., et al. 2019, *A&A*, **626**, A16
- Salaris, M., Chieffi, A., & Straniero, O. 1993, *ApJ*, **414**, 580

- Santiago, B. X., Brauer, D. E., Anders, F., et al. 2016, *A&A*, **585**, A42
- Schlafly, E. F., Meisner, A. M., Stutz, A. M., et al. 2016, *ApJ*, **821**, 78
- Scolnic, D., Casertano, S., Riess, A., et al. 2015, *ApJ*, **815**, 117
- Scott, D. W. 1992, *Multivariate Density Estimation* (New York: Wiley)
- SDSS-IV Collaboration 2019, *ApJS*, submitted [arXiv:1912.02905]
- Spitoni, E., Silva Aguirre, V., Matteucci, F., Calura, F., & Grisoni, V. 2019, *A&A*, **623**, A60
- Stassun, K. G., & Torres, G. 2018, *ApJ*, **862**, 61
- Steinmetz, M., Matijevic, G., Enke, H., et al. 2020a, *AJ*, submitted [arXiv:2002.04377]
- Steinmetz, M., Guiglion, G., McMillan, P. J., et al. 2020b, *AJ*, submitted [arXiv:2002.04512]
- Sukhbold, T., Ertl, T., Woosley, S. E., Brown, J. M., & Janka, H. T. 2016, *ApJ*, **821**, 38
- Virtanen, P., Gommers, R., Oliphant, T. E., et al. 2020, *Nat. Meth.*, **17**, 261
- Weiler, M. 2018, *A&A*, **617**, A138
- Weinberg, D. H., Holtzman, J. A., Hasselquist, S., et al. 2019, *ApJ*, **874**, 102
- Wilson, J. C., Hearty, F. R., Skrutskie, M. F., et al. 2019, *PASP*, **131**, 055001
- Woosley, S. E., Heger, A., & Weaver, T. A. 2002, *Rev. Mod. Phys.*, **74**, 1015
- Xiang, M., Ting, Y.-S., Rix, H.-W., et al. 2019, *ApJS*, **245**, 34
- Zasowski, G., Johnson, J. A., Frinchaboy, P. M., et al. 2013, *AJ*, **146**, 81
- Zasowski, G., Cohen, R. E., Chojnowski, S. D., et al. 2017, *AJ*, **154**, 198
- Zasowski, G., Finkbeiner, D. P., Green, G. M., et al. 2019, *BAAS*, **51**, 314
- Zhao, G., Zhao, Y.-H., Chu, Y.-Q., Jing, Y.-P., & Deng, L.-C. 2012, *Res. Astron. Astrophys.*, **12**, 723
- Zinn, J. C., Pinsonneault, M. H., Huber, D., & Stello, D. 2019, *ApJ*, **878**, 136
- ⁹ Millennium Institute of Astrophysics, Av. Vicuna Mackenna 4860, 782-0436 Santiago, Chile
- ¹⁰ Vatican Observatory, V00120 Vatican City State, Italy
- ¹¹ Instituto de Astrofísica de Canarias (IAC), 38205 La Laguna, Tenerife, Spain
- ¹² Universidad de La Laguna (ULL), Departamento de Astrofísica, 38206 La Laguna, Tenerife, Spain
- ¹³ Observatoire de la Côte d’Azur, Laboratoire Lagrange, 06304 Nice Cedex 4, France
- ¹⁴ The Carnegie Observatories, 813 Santa Barbara Street, Pasadena, CA 91101, USA
- ¹⁵ Department of Physics and JINA Center for the Evolution of the Elements, University of Notre Dame, Michigan State University, Notre Dame, IN 46556, USA
- ¹⁶ Apache Point Observatory, PO Box 59, Sunspot, NM 88349, USA
- ¹⁷ Sternberg Astronomical Institute, Moscow State University, Moscow, Russia
- ¹⁸ Department of Physics and Astronomy, University of Utah, 115 S. 1400 E., Salt Lake City, UT 84112, USA
- ¹⁹ University of Arizona, Tucson, AZ 85719, USA
- ²⁰ Observat’orio Nacional, Sao Cristóvão, Rio de Janeiro, Brazil
- ²¹ Institut Utinam, CNRS UMR 6213, Université Bourgogne-Franche-Comté, OSU THETA Franche-Comté, Observatoire de Besançon, BP 1615, 25010 Besançon Cedex, France
- ²² Department of Physics & Astronomy, Texas Christian University, Fort Worth, TX 76129, USA
- ²³ Instituto de Astrofísica, Pontificia Universidad Católica de Chile, Av. Vicuna Mackenna 4860, 782-0436 Macul, Santiago, Chile
- ²⁴ Instituto de Astronomía y Ciencias Planetarias, Universidad de Atacama, Copayapu 485, Copiapó, Chile
- ²⁵ Department of Astronomy, University of Virginia, Charlottesville, VA 22904-4325, USA
- ²⁶ Center for Astrophysical Sciences, Department of Physics and Astronomy, Johns Hopkins University, 3400 North Charles Street, Baltimore, MD 21218, USA
- ²⁷ Centro de Astronomía (CITEVA), Universidad de Antofagasta, Avenida Angamos 601, Antofagasta 1270300, Chile
- ²⁸ Departamento de Física, Facultad de Ciencias, Universidad de La Serena, Cisternas 1200, La Serena, Chile
- ²⁹ Department of Astronomy, University of Washington, Box 351580, Seattle, WA 98195, USA
- ³⁰ Center for Astrophysics and Space Astronomy, Department of Astrophysical and Planetary Sciences, University of Colorado, 389 UCB, Boulder, CO 80309-0389, USA
-
- ¹ Leibniz-Institut für Astrophysik Potsdam (AIP), An der Sternwarte 16, 14482 Potsdam, Germany
e-mail: aqueiroz@aip.de
- ² Laboratório Interinstitucional de e-Astronomia – LIneA, Rua Gal. José Cristino 77, Rio de Janeiro, RJ 20921-400, Brazil
- ³ Institut de Ciències del Cosmos, Universitat de Barcelona (IEEC-UB), Carrer Martí i Franquès 1, 08028 Barcelona, Spain
- ⁴ Instituto de Física, Universidade Federal do Rio Grande do Sul, Caixa Postal 15051, Porto Alegre, RS 91501-970, Brazil
- ⁵ School of Physics and Astronomy, University of Birmingham, Edgbaston, Birmingham B15 2TT, UK
- ⁶ Centro de Astrofísica da Universidade do Porto, Rua das Estrelas 4150-762, Porto, Portugal
- ⁷ Department of Astronomy, Universidade de São Paulo, São Paulo 05508-090, Brazil
- ⁸ Departamento de Ciencias Físicas, Facultad de Ciencias Exactas, Universidad Andres Bello, Av. Fernandez Concha 700, Las Condes, Santiago, Chile

Appendix A: StarHorse data model

The tables in this appendix describe our data model for the APOGEE DR16 StarHorse VAC (Table A.1) and the

meaning of the human-readable flags SH_INPUTFLAGS and SH_OUTPUTFLAGS (Table A.2).

Table A.1. Data model for the StarHorse catalogues described in this paper.

Column	Description	Unit
ID	Unique object identifier	string
glon	Galactic longitude	deg
glat	Galactic latitude	deg
mass16	16th percentile of StarHorse stellar mass PDF	M_{\odot}
mass50	50th percentile of StarHorse stellar mass PDF	M_{\odot}
mass84	84th percentile of StarHorse stellar mass PDF	M_{\odot}
teff16	16th percentile of StarHorse effective temperature PDF	K
teff50	50th percentile of StarHorse effective temperature PDF	K
teff84	84th percentile of StarHorse effective temperature PDF	K
logg16	16th percentile of StarHorse surface gravity PDF	dex
logg50	50th percentile of StarHorse surface gravity PDF	dex
logg84	84th percentile of StarHorse surface gravity PDF	dex
met16	16th percentile of StarHorse metallicity PDF	dex
met50	50th percentile of StarHorse metallicity PDF	dex
met84	84th percentile of StarHorse metallicity PDF	dex
dist16	16th percentile of StarHorse distance PDF	kpc
dist50	50th percentile of StarHorse distance PDF	kpc
dist84	84th percentile of StarHorse distance PDF	kpc
AV16	16th percentile of StarHorse extinction in the V band PDF	mag
AV50	50th percentile of StarHorse extinction in the V band PDF	mag
AV84	84th percentile of StarHorse extinction in the V band PDF	mag
SH_INPUTFLAGS	StarHorse flags specifying catalogue input completeness and quality	string
SH_OUTPUTFLAGS	StarHorse flags specifying output quality	string

Table A.2. Description of the contents of the StarHorse flags.

SH_INPUTFLAGS	Description
“TEFF..”	Calibrated spectroscopic parameters (e.g. TEFF) were used
“uncalTEFF..”	Uncalibrated spectroscopic parameters (e.g. TEFF) + inflated uncertainties were used
“PARALLAX”	<i>Gaia</i> DR2 parallaxes + recalibrated zeropoint and uncertainties were used
“ <i>JHKs</i> ”	2MASS photometry was used
“W1W2”	WISE photometry was used
“ <i>BVgr</i> ”	APASS photometry was used
“gps1_rps1..”	PanSTARRS-1 photometry was used
“AV_prior”	Extinction prior (e.g. from APOGEE targeting) was used
SH_OUTPUTFLAGS	
“NEGATIVE_EXTINCTION”	Bad extinction estimates
“NUMMODELS_HIGH”	High number of stellar models compatible with observations within 3σ
“NUMMODELS_LOW”	Low number of stellar models compatible with observations within 3σ

Appendix B: Validation

At the level of spectroscopic stellar surveys, it is difficult to perform truly independent benchmark tests for the resulting distance, extinction, and stellar parameter scales (Jofré et al. 2019). Most comparison samples are themselves affected by significant systematic uncertainties. Especially for the APOGEE survey, meaningful comparisons with fundamental physical parameters such as interferometric temperatures or masses of detached eclipsing binaries are unavailable. In Santiago et al. (2016) and Q18 we performed fundamental accuracy and precision tests using simulated stars, nearby eclipsing binaries, astrometric distances, among others. In this section we therefore limit our validation to new, but slightly less fundamental tests: consistency with input parallaxes, asteroseismology (using the CoRoT-APOGEE sample), open clusters (using *Gaia* DR2 results), an inter-survey comparison, and a comparison with results obtained by Leung & Bovy (2019).

B.1. Comparison to input parallaxes

As a first simple consistency check, we show in Fig. B.1 a comparison between our spectro-photo-astrometric distances with the recalibrated *Gaia* DR2 input parallaxes. We canonically allow StarHorse to converge to a solution that deviates from the input measurements by maximum 4σ , using trimmed Gaussians in the likelihood computation. We therefore expect an almost perfect agreement with the input parallaxes within the corresponding uncertainties. Figure B.1 shows that this expectation is fulfilled. The top panel compares our posterior estimates with the naive $1/\varpi$ distances (which is biased estimator of the true distance; see Luri et al. 2018), while the bottom panel demonstrates that there are minimal residuals between the input and the posterior parallaxes within the *Gaia* DR2 parallax sphere (the region where parallax uncertainties are within 10–15%; $d \lesssim 2.5$ kpc). We only see slight systematic trends appearing for distances $d \gtrsim 10$ kpc. In the regime in between, the parallax information is successfully complemented by APOGEE, delivering less biased and more precise StarHorse distances.

B.2. Asteroseismology: The CoRoT-APOGEE sample

In Fig. B.2 we show a direct comparison of the distances, A_V , and surface gravity for stars in common between the APOGEE DR16 StarHorse results and the CoRoGEE sample (Anders et al. 2017b), which contains stars observed by both APOGEE and the CoRoT space mission (Baglin et al. 2006). The CoRoT data allow us to determine stellar masses and radii from asteroseismology, thus also providing more precise distances outside the *Gaia* parallax sphere.

A similar comparison was shown in Sect. 5.2 of Q18, but the present comparison is significantly different in two ways: First, the CoRoGEE distances were obtained with an updated version of the PARAM code (Rodrigues et al. 2017), which has a configuration in which the input parameters were the two seismic parameters ($\Delta\nu$ and ν_{\max}) and the APOGEE DR16 temperatures, metallicities, and $[\alpha/\text{Fe}]$ values. No *Gaia* parallaxes were used. Second, in contrast to the StarHorse run shown in Fig. 9 of Q18 (which used the PARAM distances as an input), we now compare to the StarHorse results obtained without any input from neither asteroseismology nor PARAM. In summary, we compare the result of two independent distance codes, one of which uses spectroscopy and asteroseismology (PARAM), and the other uses spectroscopy and astrometry (StarHorse).

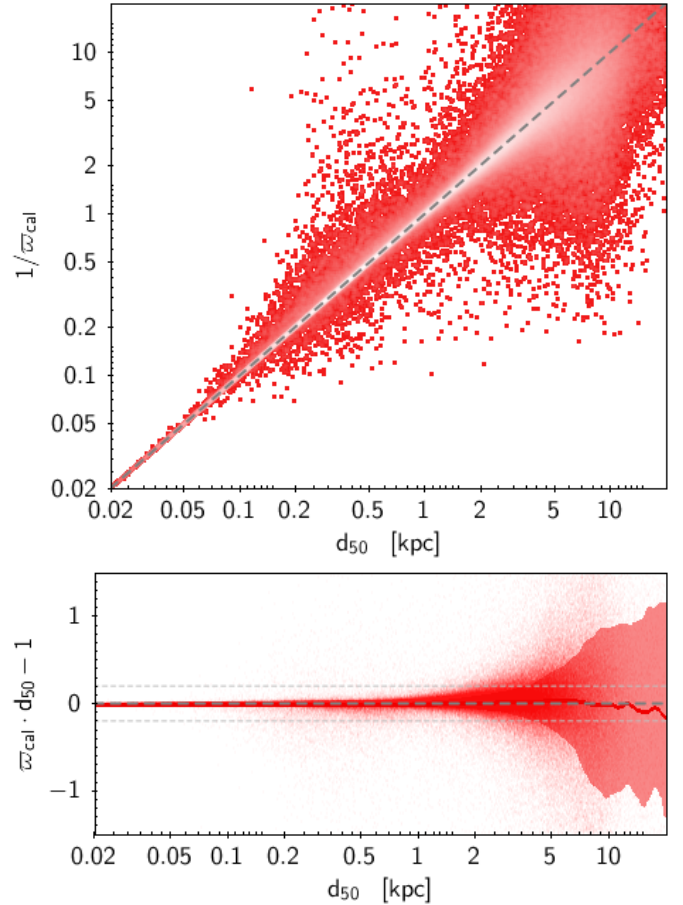


Fig. B.1. Comparison of StarHorse DR16 distances to naive distances obtained by inverting the recalibrated *Gaia* DR2 parallaxes. *Top panel:* one-to-one comparison of posterior with naive $1/\varpi$ distances. *Bottom panel:* residuals between pure astrometric and spectro-photo-astrometric ($1/d_{50}$) parallaxes. The red line shows the smoothed running median, while the shaded region shows the corresponding 1σ variations.

In Fig. B.3 we show the comparisons between the input temperatures from APOGEE DR16 and the output temperatures from PARAM and StarHorse codes. We see a systematic shift between PARAM and APOGEE DR16 temperatures even for PARAM tension flags equal zero. In contrast to PARAM, StarHorse output temperatures are very similar from the APOGEE input, since the spectroscopic errors are small and StarHorse does not rely on the seismic information. The systematic difference in temperatures between PARAM and APOGEE maybe due to the different calibration scales and model choices, which in the case of PARAM is MESA (Paxton et al. 2011).

Considering this systematic shift between PARAM output temperatures and APOGEE DR16, and looking at simulation tests with StarHorse (see Fig. 6 of Q18, bottom left panel), we expect a shift in the extinction itself, which is seen in the left top panel of Fig. B.2. The magnitude of this shift in the extinction scale, however, exceeds our expectation: for a systematic +50 K shift in T_{eff} we would expect not more than 0.1 mag difference in extinction. We therefore tentatively attribute this difference to the missing reliable optical photometry for the APOGEE DR16 sample. Distances and superficial gravity are in very good agreement with those derived by PARAM using asteroseismic measurements.

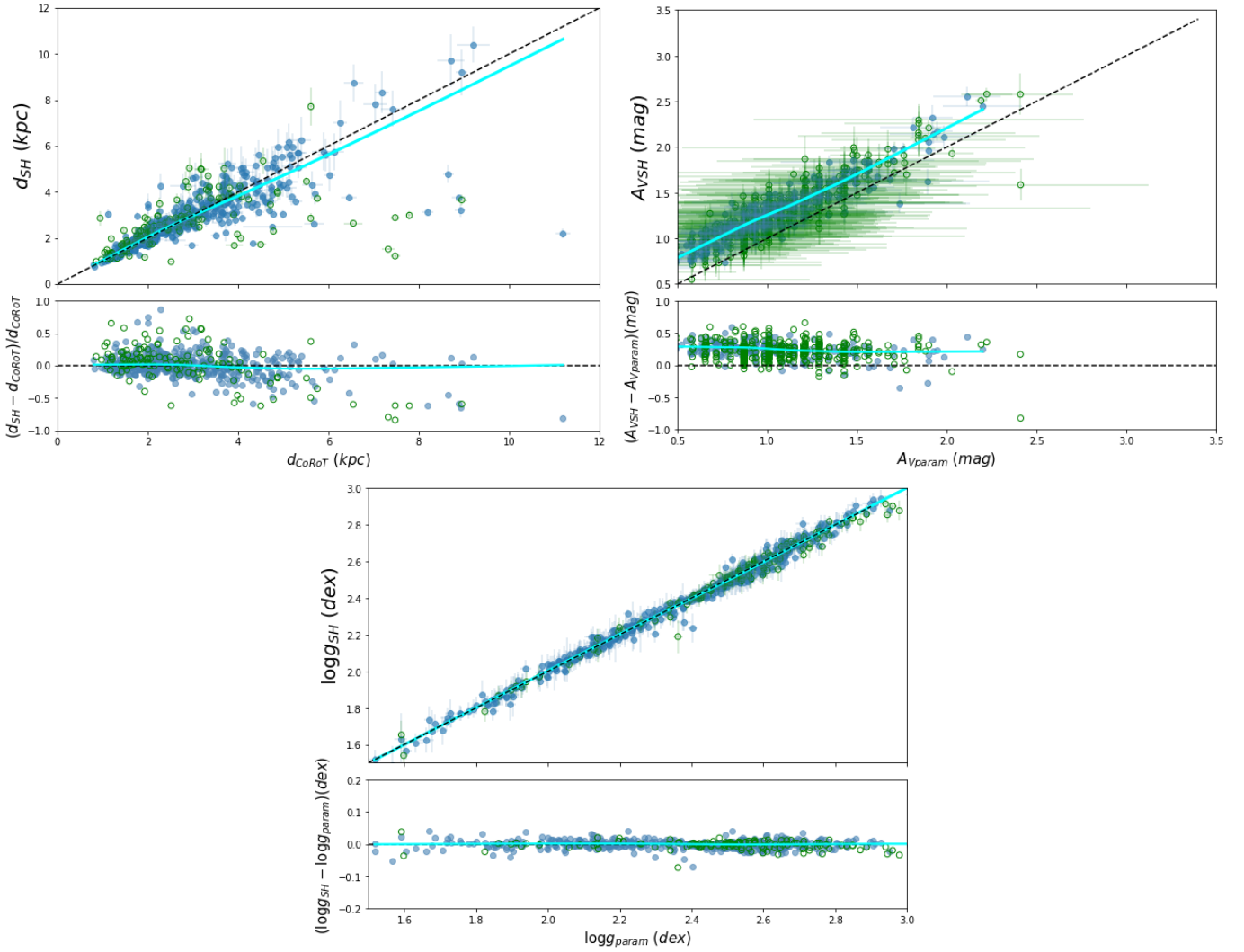


Fig. B.2. Comparison between distances and extinctions obtained in this work and those obtained from asteroseismology for CoRoT stars with APOGEE spectra (CoRoGEE sample) using an updated version of the PARAM code (Rodrigues et al. 2017). Blue filled dots are all stars with PARAM tension flags equal zero, for which the PDF of the estimated quantities does not contain multiple peaks. The cyan line indicates the locally linear adjust of the blue filled dots. In the case of extinction, *right top panel*, the blue dots represents the subset of PARAM tension flags equal zero and stars for which all photometric filters were available. Green open symbols indicate all stars that do not satisfy the conditions of the blue dots.

B.3. Open clusters

In A19, we present a detailed comparison of StarHorse results (without using spectroscopic data) with open-cluster parameters derived from *Gaia* DR2 data (specifically, Cantat-Gaudin et al. 2018; Bossini et al. 2019). Cantat-Gaudin et al. (2018) determine membership probabilities for 1229 Galactic open clusters, while Bossini et al. (2019) publish revised Bayesian cluster parameters for 269 of those clusters, based on the same membership list. In this work we again compare with the results obtained by Bossini et al. (2019), keeping in mind now that the APOGEE DR16 StarHorse results were obtained from higher-quality data.

In Fig. B.4, we compare the APOGEE StarHorse results obtained for the most certain cluster members of Cantat-Gaudin et al. (2018) to the distances and extinctions determined similar to Bossini et al. (2019) with same input photometry as we use in StarHorse and using PARSEC models in the PARAM code. The figure shows a cluster-by-cluster comparison for the 12 most populated clusters observed by APOGEE, ordered by distance. In general, and in accordance with A19, we observe good agreement of the distance scales (within 20%). Some discrepancies

are noticeable both in extinction and distance, which could be related to differential reddening, impure membership, and bad photometry, although this is mostly within the accuracy limits of the open cluster distance scale of Bossini et al. (2019). For the closest clusters, we see a very strong systematic difference in extinction estimates (up to >1 mag). Its origin, however, is different from the shift seen in the comparison with the CoRoGEE sample: the ASPCAP T_{eff} scale of the M dwarf stars is offset from the PARSEC scale by over 200 K, thus forcing StarHorse to converge to a solution with higher extinction (see Q18, Fig. 6).

B.4. Inter-survey comparison

Some of the stars observed by APOGEE have also been observed by other spectroscopic surveys, be it as a part of a dedicated cross-calibration effort or by chance. These stars are also useful to test the consistency of the StarHorse results. Therefore, in Fig. B.5 we show the distribution of differences in StarHorse output parameters for stars co-observed by APOGEE DR16 and LAMOST DR5, GALAH DR2, RAVE DR6, and GES DR3,

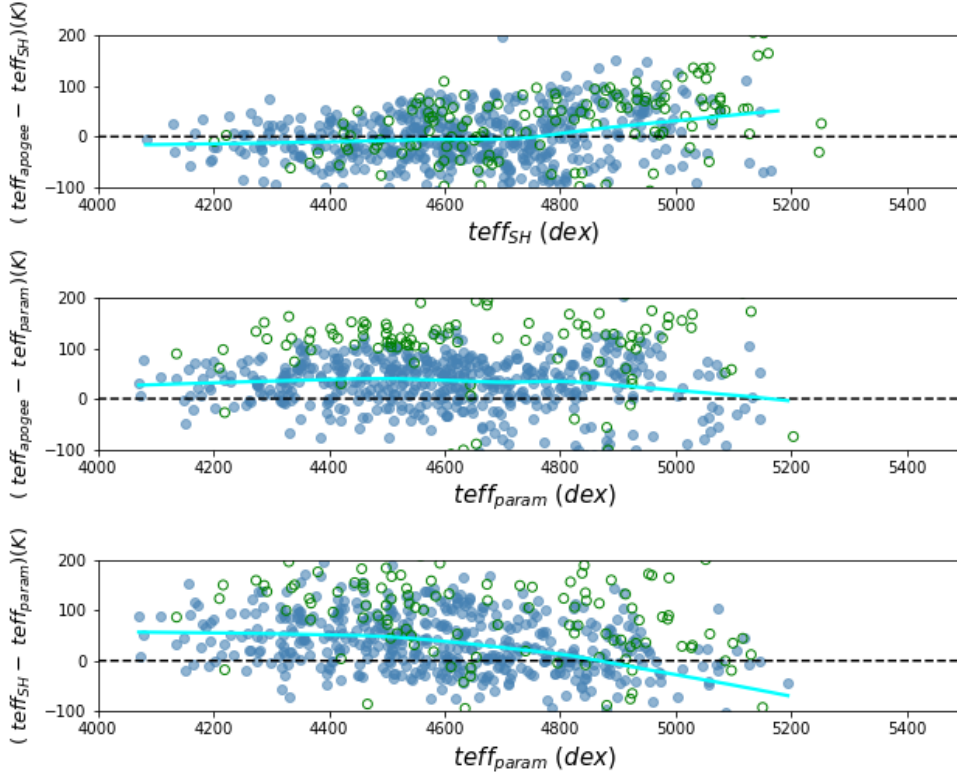


Fig. B.3. Comparison between temperatures from APOGEE DR16, the output PARAM code, and output StarHorse. Blue filled dots indicate all stars with PARAM tension flags equal zero, for which the PDF of the estimated quantities does not contain multiple peaks. The cyan line represents the locally linear adjust of the blue filled dots. Green open symbols indicate all stars that do not satisfy the conditions of the blue dots.

Comparison to Bossini et al. (2019) cluster distances and extinctions

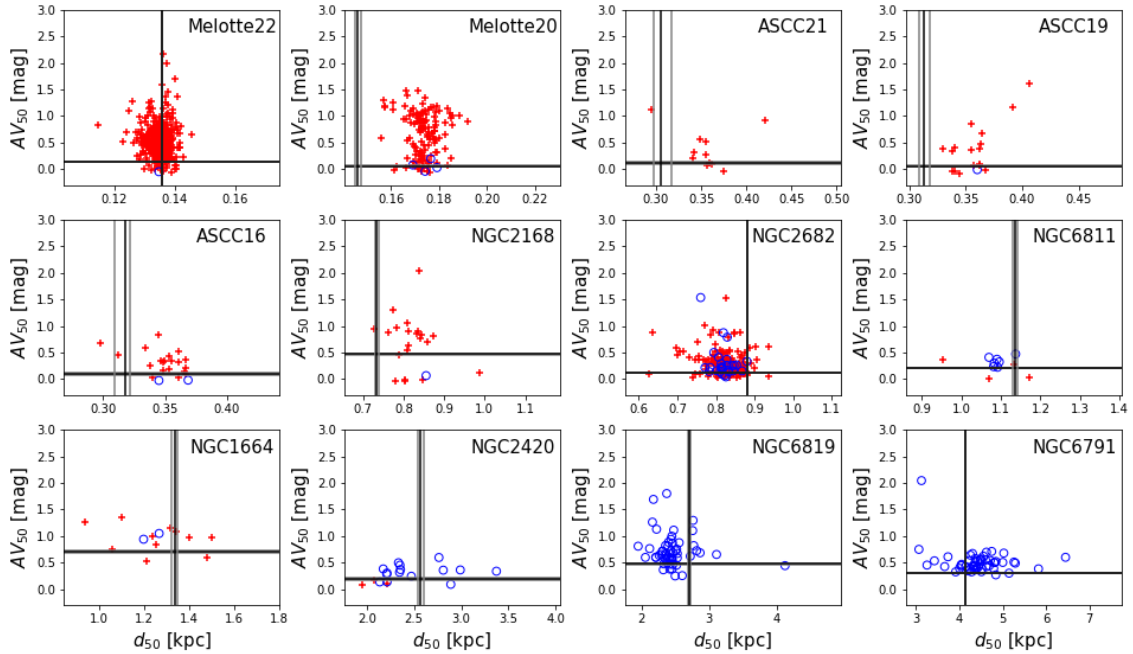


Fig. B.4. Comparison between distances and extinctions obtained in this paper with those obtained by Bossini et al. (2019), but in this case for the same input photometry as StarHorse and with PARSEC models, for open clusters. Each panel corresponds to an open cluster with more than ten member candidates observed by APOGEE. The median StarHorse results for individual stars in each cluster are shown as red crosses (dwarfs) and blue open circles (giants). The horizontal and vertical lines correspond to the median values and 1σ limits inferred by Bossini et al. (2019) through isochrone fitting.

respectively (using simple cross-matches based on the *Gaia* DR2 source_id), colour-coded in the same way as Figs. 10 and 11. The distances obtained from the different input spectroscopic parameters show very satisfactory consistency (first row

of Fig. B.5), with systematics at the 1–2%-level, and standard deviations typically below the quoted uncertainties.

In accordance with the previous tests above, the extinction comparison for the survey overlap stars (second row of Fig. B.5)

Survey overlap comparison

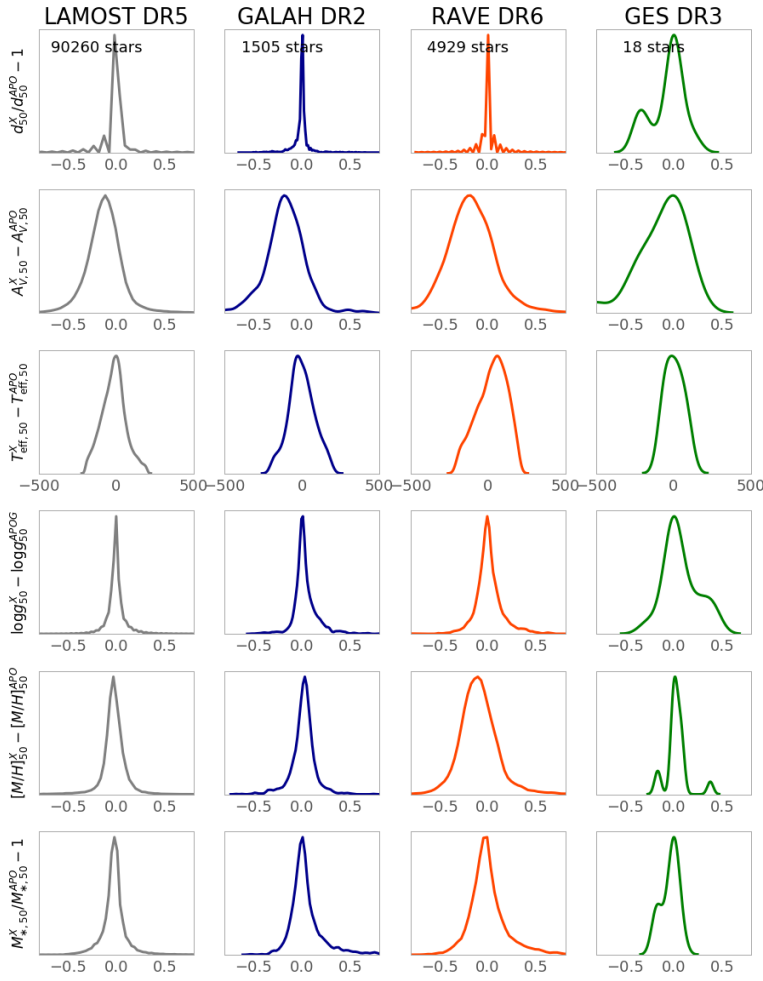


Fig. B.5. Inter-survey comparison of the derived StarHorse results using stars co-observed by APOGEE and LAMOST (left column), GALAH (second column), RAVE (third column), and GES (fourth column). Each panel shows a generalised histogram of differences of the posterior parameters obtained by StarHorse indicated in the y-axis of each row. For each survey, the number of stars in common with APOGEE DR16 is given in the top panel.

shows that the APOGEE DR16 extinctions are on a slightly offset scale with respect to those obtained from LAMOST DR5, GALAH DR2, and RAVE DR6. As explained above, we suggest this to be due to a combination of a slight systematic offset of the ASPCAP T_{eff} scale with respect to that of the PARSEC models, and the missing reliable optical photometry for most of the DR16 sample.

The comparison of the other StarHorse output parameters (T_{eff} , $\log g$, $[M/H]$, and mass) is shown in the bottom rows of Fig. B.5, showing a very satisfactory agreement in the parameter scales of the different surveys.

B.5. astroNN distances

Finally, in Fig. B.6 we compare our APOGEE DR16 distances with those obtained with the neural-network spectral analysis code astroNN (Leung & Bovy 2019). These authors claimed that “there is no doubt that our distances have higher precision and accuracy than those determined using stellar models and density priors, such as the BPG distances”, based on a comparison with the pre-*Gaia* distances published in Santiago et al.

(2016) prior to *Gaia*. In this appendix we repeat their comparison with our new results, now including *Gaia* DR2, revealing a more complex picture.

The top left panel of Fig. B.6 shows that there is a generally very good agreement between the distances derived by the two codes for the bulk of the sample up to ~ 10 kpc (density colour coding in this plot is logarithmic). There are, however, groups of stars which deviate considerably from the one-to-one relation: First, dwarf stars located mostly at high latitudes (see $\log g$ -coloured plot in the top right panel and sky distribution of distance residuals in the bottom left panel) for which astroNN determines too high distances (compare to Fig. B.1), and second, giant stars in the inner Galaxy, for which systematic differences of the order of 10–20% are visible (in the sense that the Leung & Bovy 2019 distances are significantly smaller; see bottom right panel).

The first group of stars can be explained by the limited training set used by Leung & Bovy (2019), which were comprised almost exclusively of red-giant stars. The second effect was indeed also noticed by Bovy et al. (2019) who corrected the systematic offset of the astroNN distances heuristically (see their Fig. 1).

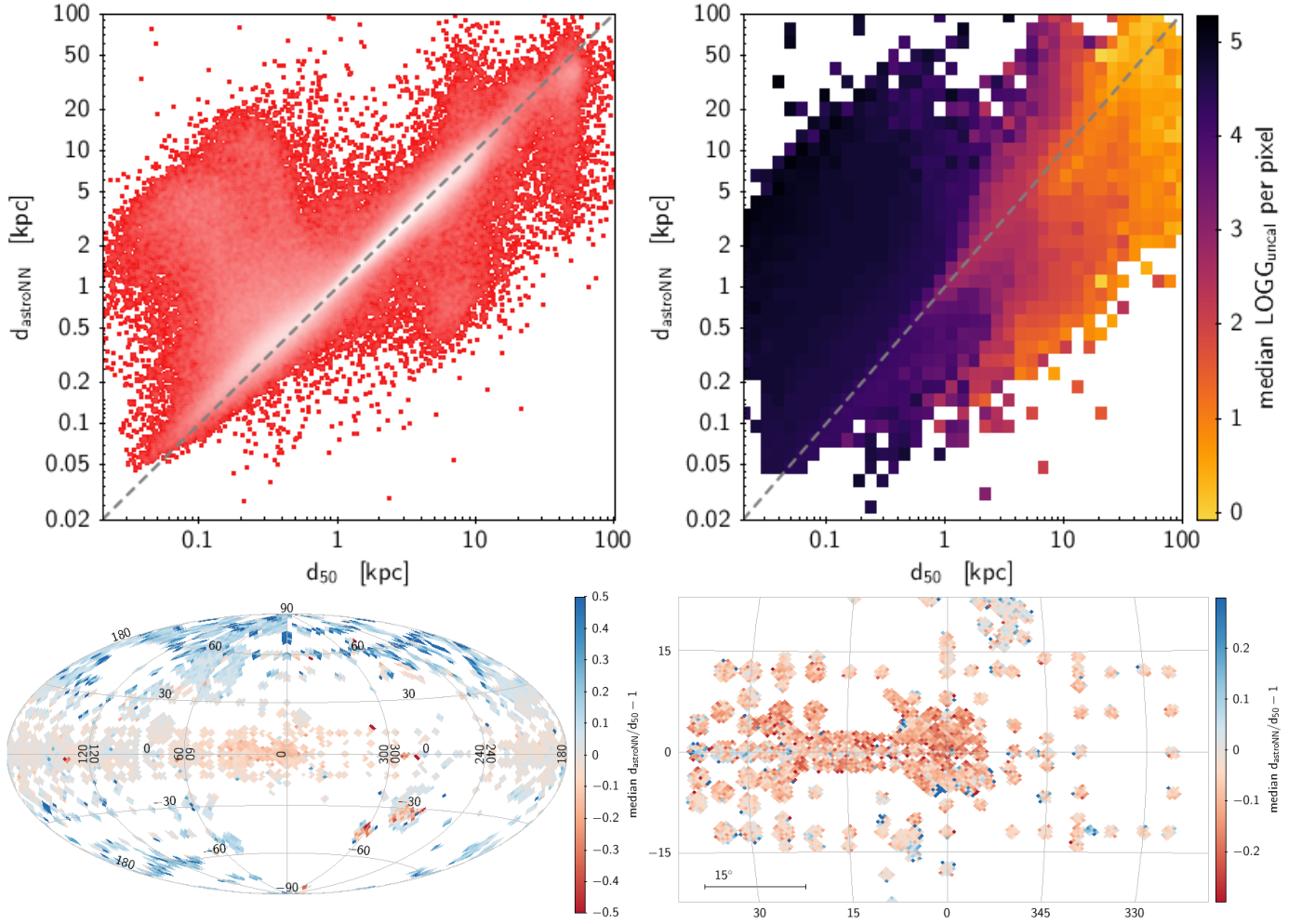


Fig. B.6. Comparison with astroNN distances presented by Leung & Bovy (2019). *Top panel:* 1-to-1 comparison (*left:* density distribution; *right:* colour-coded by median uncalibrated surface gravity determined by ASPCAP, showing that astroNN is overestimating distances to dwarf stars). *Bottom panels:* relative distance differences as a function of sky position (*left:* whole sky, *right:* zoom into the inner Galaxy).

Appendix C: Summary plots for GALAH, RAVE, GES, and LAMOST

In this section, we show some summary figures illustrating the quality of our new StarHorse results for the surveys considered in this paper in addition to the APOGEE DR16 results. In particular, in Figs. C.1 through C.4 we provide sky plots and

Kiel diagrams and CMDs for LAMOST DR5, GALAH DR2, RAVE DR6, and GES DR3, similar to Figs. 2 and 3. Figures C.5 through C.8 display summary corner plots of the StarHorse output parameters for each survey, as shown for APOGEE DR16 in Fig. 1. The colour in each of those plots coincides with the colours used in Figs. 10 and 11.

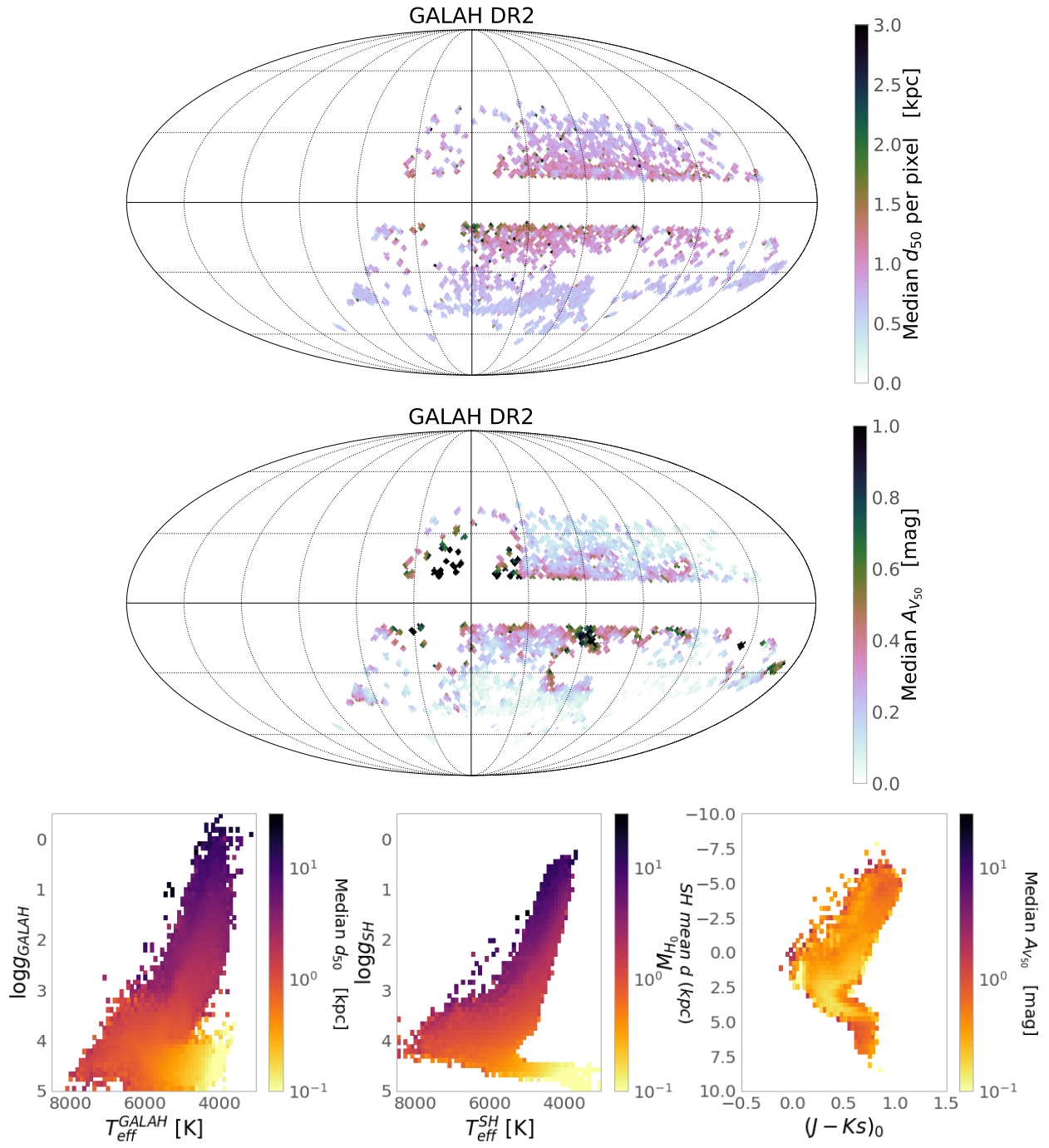


Fig. C.1. Similar to Figs. 2 and 3, but now for GALAH DR2.

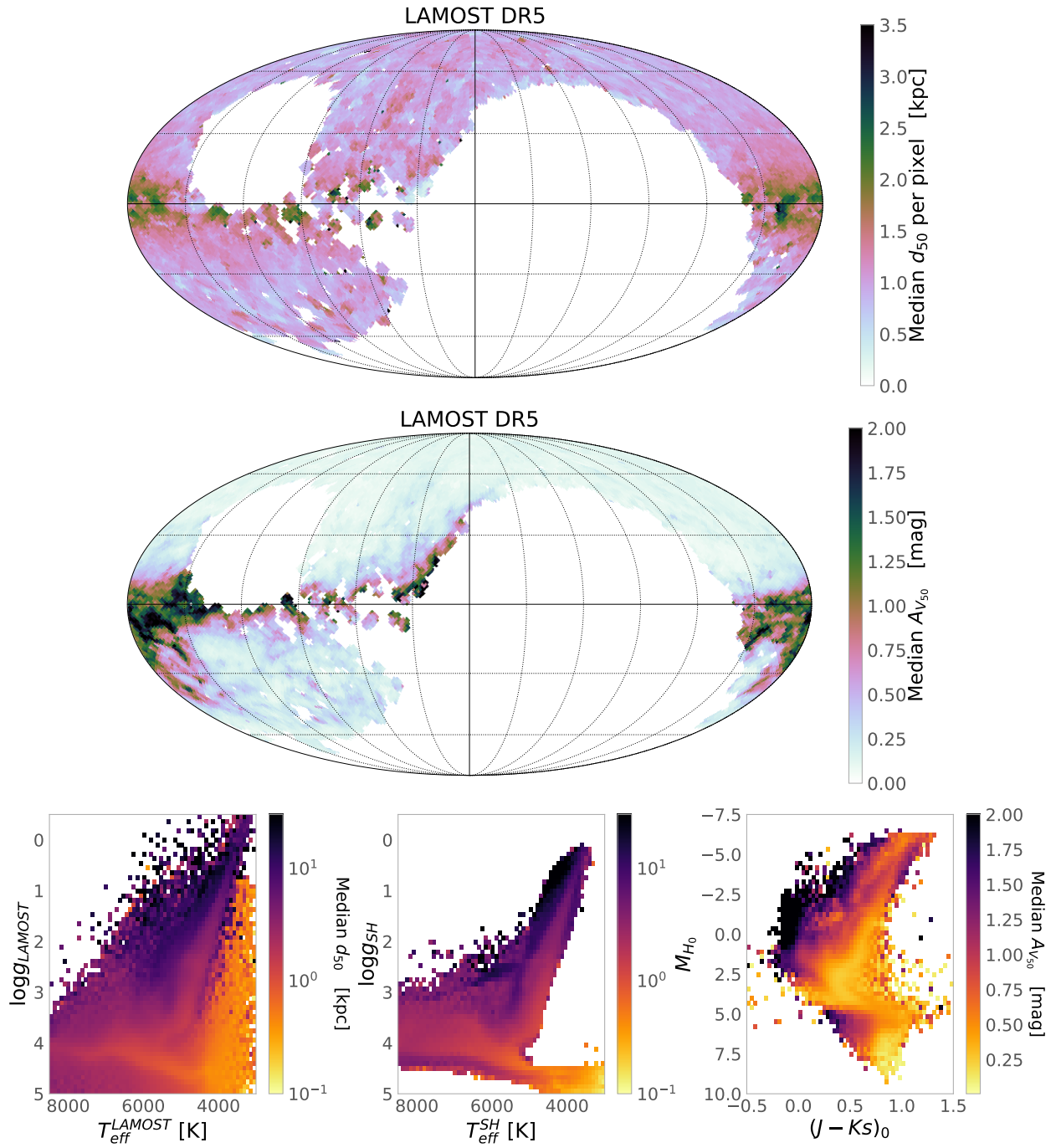


Fig. C.2. Similar to Figs. 2 and 3, but for LAMOST data. The CMD shown in the *right panel* does not include sources fainter than $K_s = 14.5$.

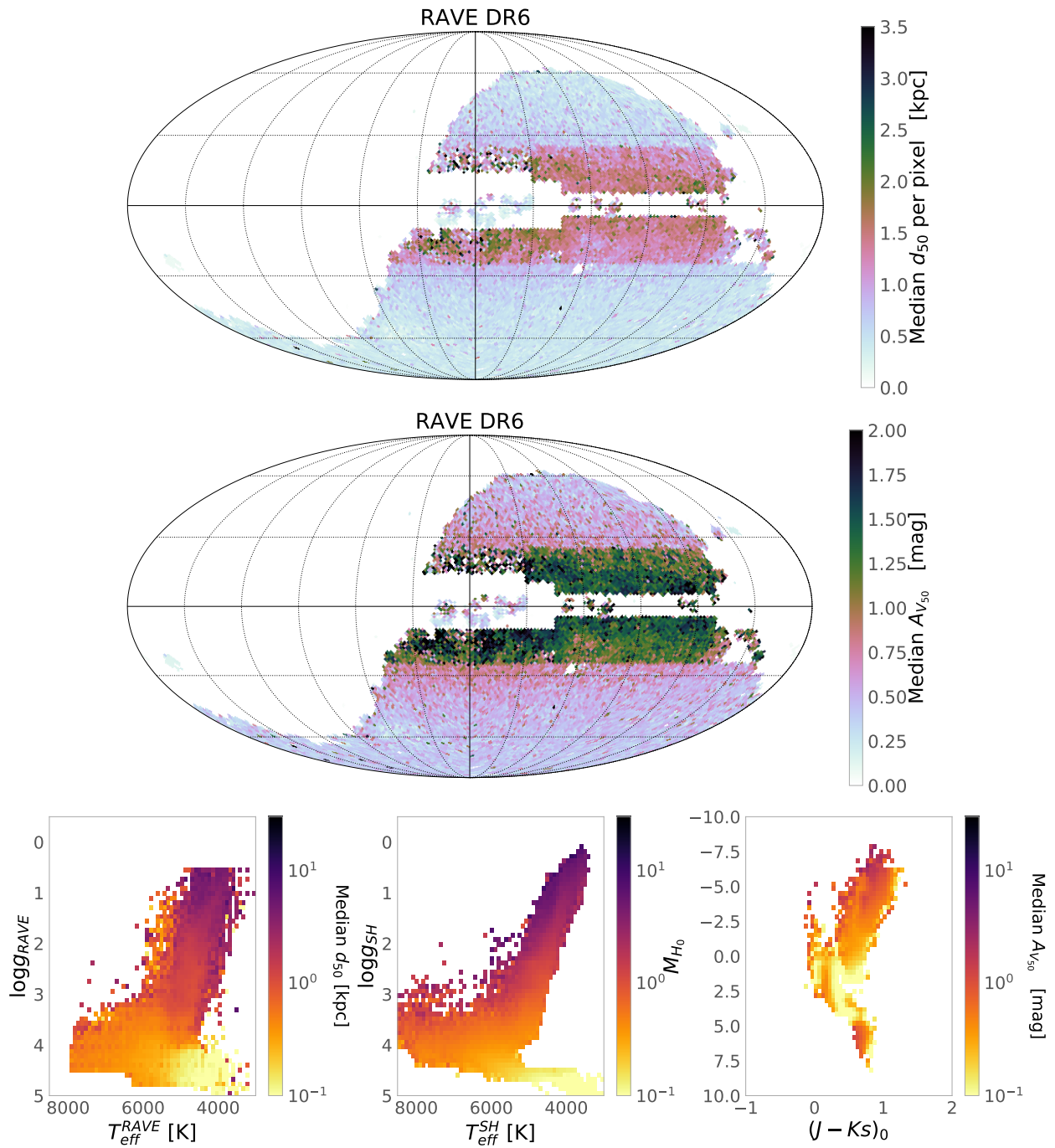


Fig. C.3. Similar to Figs. 2 and 3, but for RAVE DR6 data.

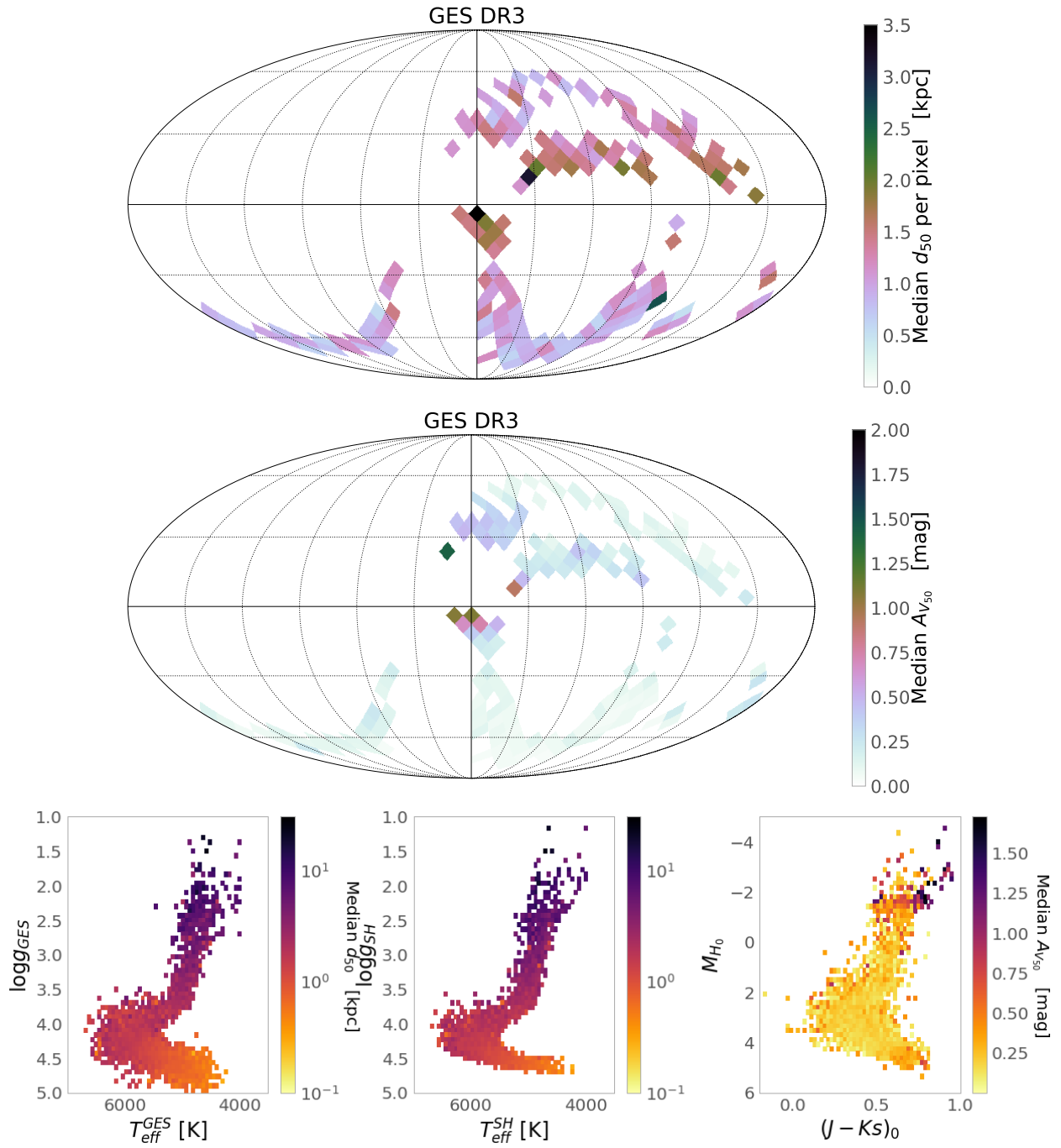


Fig. C.4. Similar to Figs. 2 and 3, but for GES DR3 data.

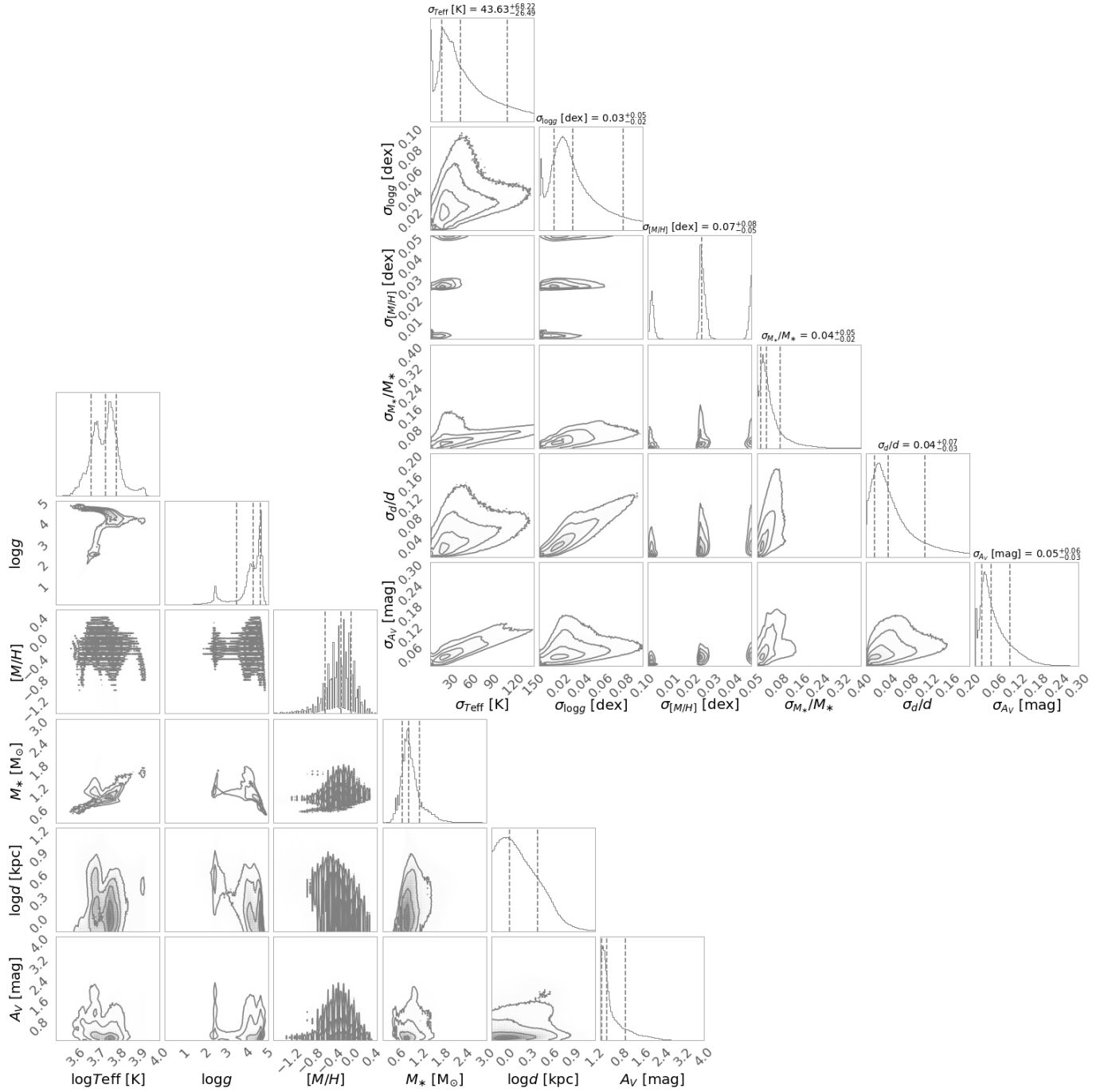


Fig. C.5. 1D distributions and correlations between StarHorse output parameters (*bottom left corner plot*) and their corresponding uncertainties (*top right corner plot*) for the LAMOST DR5 VAC sample.

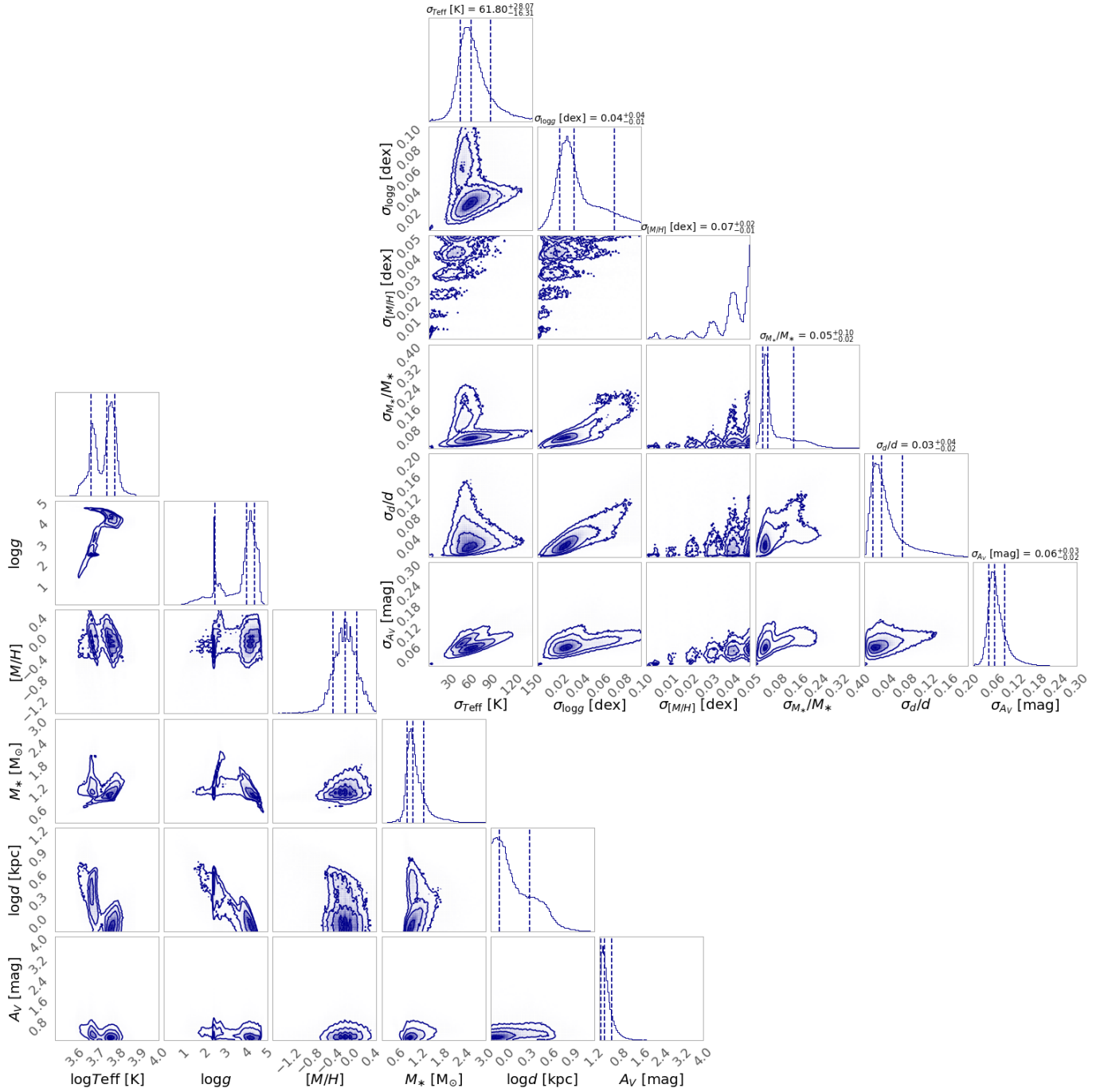


Fig. C.6. 1D distributions and correlations between StarHorse output parameters (*bottom left corner plot*) and their corresponding uncertainties (*top right corner plot*) for the GALAH DR2 sample.

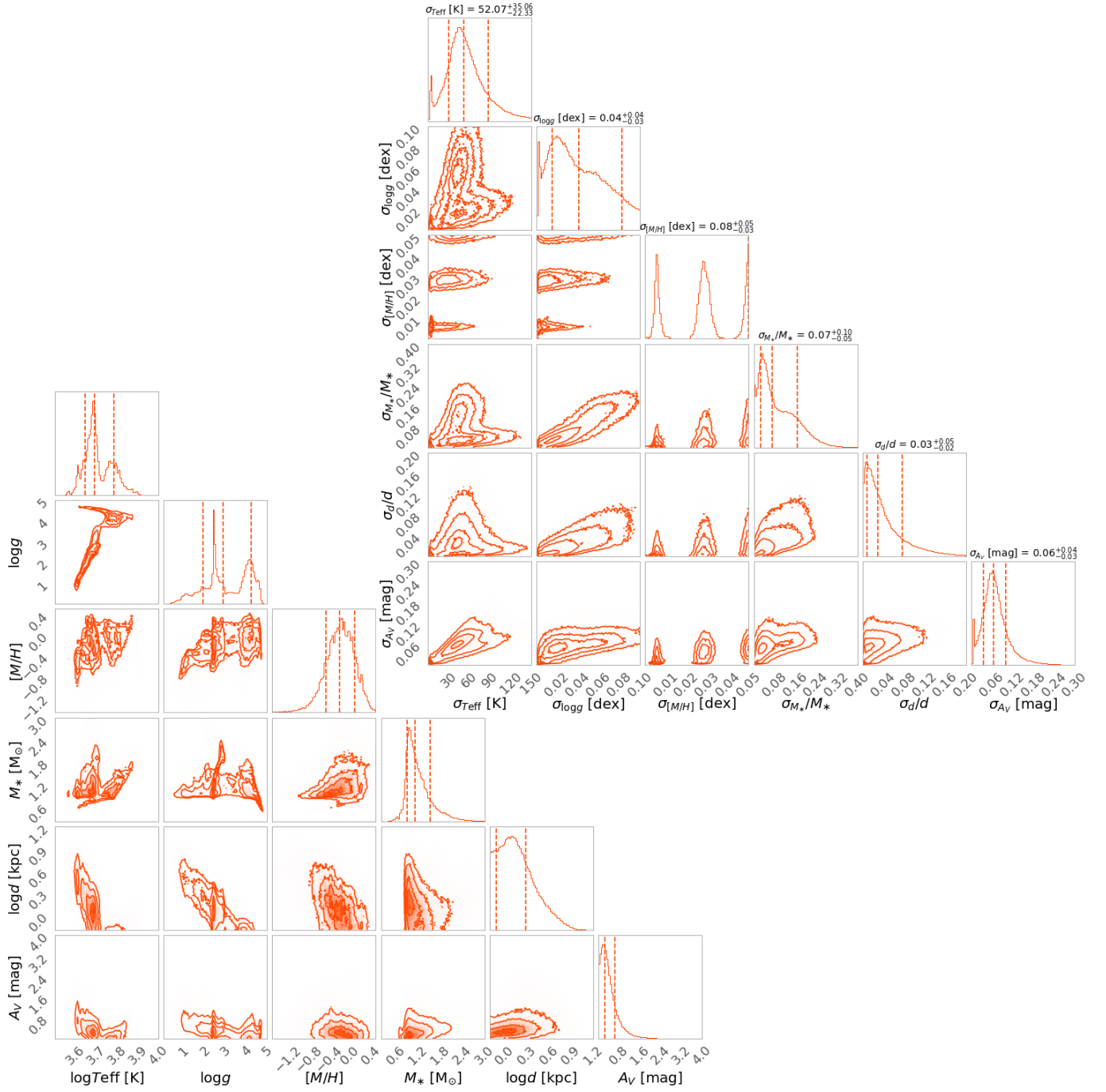


Fig. C.7. 1D distributions and correlations between StarHorse output parameters (*bottom left corner plot*) and their corresponding uncertainties (*top right corner plot*) for the RAVE DR6 sample.

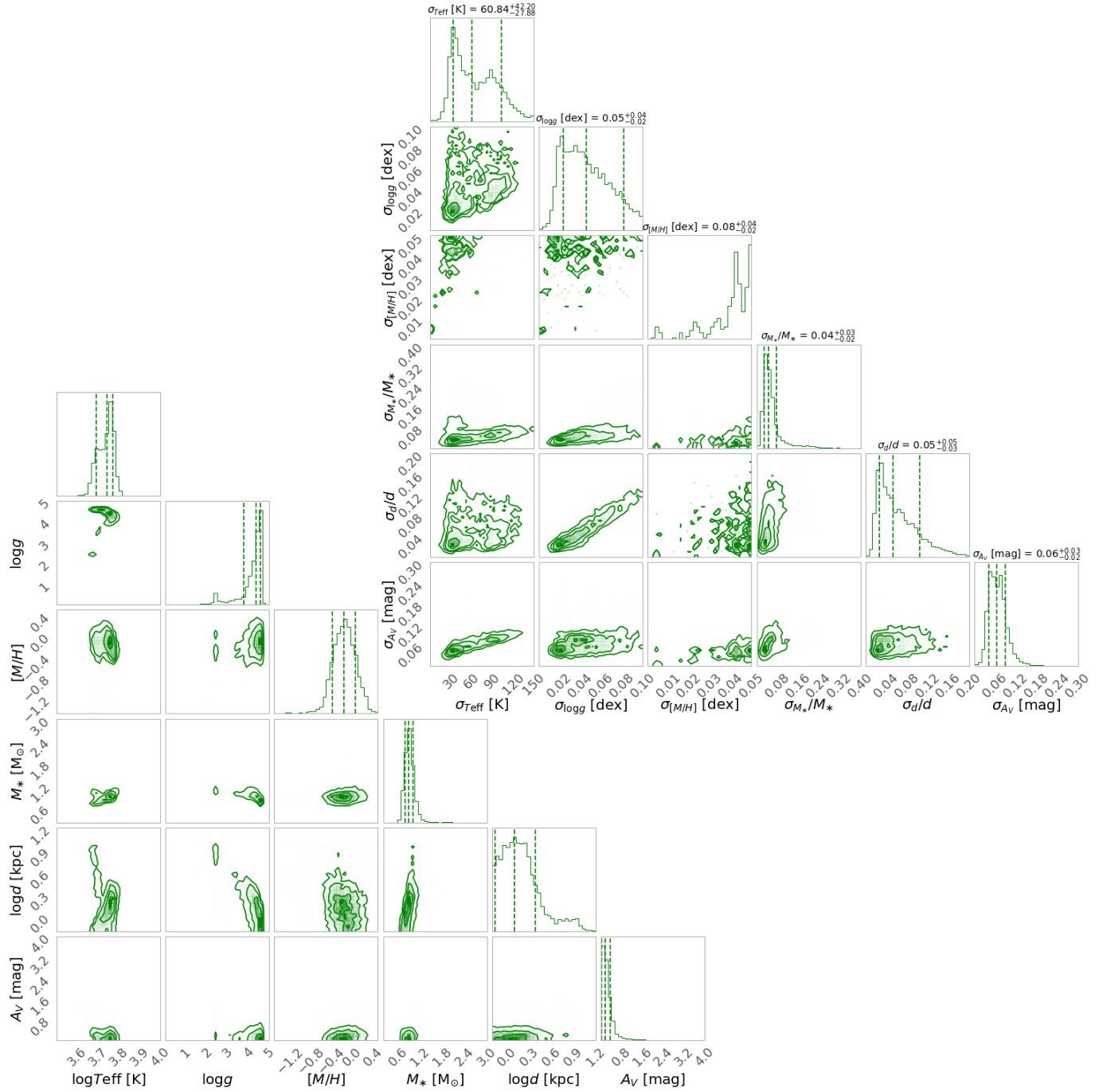


Fig. C.8. 1D distributions and correlations between StarHorse output parameters (*bottom left corner plot*) and their corresponding uncertainties (*top right corner plot*) for the GES DR3 sample.